

# Efficient representation of spatio-temporal data using cylindrical shearlets

Tatiana A. Bubba<sup>a</sup>, Glenn Easley<sup>b</sup>, Tommi Heikkilä<sup>c</sup>, Demetrio Labate<sup>d,\*</sup>,  
Jose P. Rodriguez Ayllon<sup>e</sup>

<sup>a</sup>*Department of Applied Mathematics and Theoretical Physics, University of Cambridge, Wilberforce Rd, Cambridge CB3 0WA, United Kingdom*

<sup>b</sup>*Applied Physics Laboratory, Johns Hopkins University, 11100 Johns Hopkins Road Laurel, Maryland 20723, USA*

<sup>c</sup>*Department of Mathematics and Statistics, University of Helsinki, Pietari Kalmin katu 5, 00014 Helsinki, Finland*

<sup>d</sup>*Department of Mathematics, University of Houston, 651 Phillip G Hoffman Houston, Texas 77204-3008, USA*

<sup>e</sup>*Universidad Mayor de San Andres, Av. Villazon 1995 Monoblock Central, La Paz, Bolivia*

---

## Abstract

Efficient representations of multivariate functions are critical for the design of state-of-the-art methods of data restoration and feature extraction. In this work, we consider the representation of spatio-temporal data such as temporal sequences (videos) of 2- and 3-dimensional images, where conventional separable representations are usually very inefficient, due to their limitations in handling the geometry of the data. To address this challenge, we consider an idealized class  $\mathcal{E}(A) \subset L^2(\mathbb{R}^4)$  of functions of 4 variables dominated by hypersurface singularities in the first three coordinates that we apply to model 4-dimensional data corresponding to temporal sequences (videos) of 3-dimensional objects. To provide an efficient representation for this type of data, we introduce a new multiscale directional system of functions based on cylindrical shearlets and prove that this new approach achieves superior approximation properties with respect to conventional multiscale representations. To further illustrate the advantages of our approach, we apply a discrete implementation of the new representation to problems of dynamic tomography using synthetic data.

*Keywords:* dynamic tomography, multiscale analysis, shearlets, spatio-temporal data, sparse approximations, regularization

*2010 MSC:* 42C10, 42C40, 92C55, 47A52

---

\*Corresponding author

*Email address:* [dlabate@math.uh.edu](mailto:dlabate@math.uh.edu) (Demetrio Labate)

## 1. Introduction

Sparse representations of multivariate functions have been remarkably successful in applied mathematics and signal processing, with several applications ranging from image denoising and inpainting through medical image reconstruction and feature extraction being proposed during the last decade. A multiplicity of such constructions were introduced to deal with different types of multidimensional data and signal processing tasks, including curvelets [1], shearlets [2, 3], bandlets [4], scattering wavelets [5], bendlets [6], parabolic molecules [7], directional multivariate wavelets [8] and directional framelets [9]. The key observation underpinning such constructions is that representations of multivariate functions must be able to capture the fundamental geometric data features to provide superior approximation properties and hence offer the potential for useful signal processing applications. For instance, shearlets, which are defined as countable collections of well localized anisotropic waveforms on  $L^2(\mathbb{R}^2)$  ranging over multiple scales, location and orientations, are especially designed to represent edge discontinuities. As a result, they provide optimally sparse approximations, in a precise sense, for cartoon-like images - a class of piecewise smooth functions that is used to model a large class of natural images - outperforming conventional multiscale representations. Such approximation properties were critically exploited to develop a number of very successful applications from signal processing and medical imaging [10, 11, 12, 13, 14].

In this paper, we introduce a new construction of *cylindrical shearlets* on  $L^2(\mathbb{R}^4)$  aimed at the efficient representation of spatio-temporal data, that is, temporal sequences (or videos) of 3-dimensional objects. Our approach is especially motivated by dynamic computed tomography (CT), a medical imaging technique whose goal is to reconstruct 3-dimensional image sequences where the main focus is the dynamic of the living human body [15] for applications such as cardiac imaging or image-guided interventional medical procedures. A main challenge in dynamic CT reconstruction is that, due to technical or physical constraints, data are often heavily undersampled causing the inverse problem associated with the reconstruction task to be potentially ill-posed. For instance, many dynamic CT scenarios involve the use of contrast tracers and full X-ray scans are too slow to capture the movement of the tracer (e.g., iodine) in the imaging windows. The most common remedy for reducing the duration of the imaging as well as the radiation dose consists in lowering the number of scanning angles leading to an undersampled reconstruction problem.

Some of the authors of this paper have recently shown that one can successfully address the undersampled reconstruction problem in dynamic CT by taking advantage of appropriate sparse data representations [16]. In particular, 3-dimensional shearlets were successfully applied to develop an improved algorithm for the reconstruction of 2-dimensional time frames in sparse dynamic tomography by exploiting their superior approximation properties of 3-dimensional data. However, their method does not apply directly to the ‘full’ dynamic CT problem of reconstructing 3-dimensional time frames, that is, 4-dimensional data. To deal with such task, here we introduce cylindrical shear-

lets on  $L^2(\mathbb{R}^4)$  as a collection of well-localized waveforms ranging over multiple scales, locations and orientations on  $\mathbb{R}^4$ . To better adapt the geometry of this representation to the characteristics of spatio-temporal data - under the simplifying assumptions that such data are dominated by hyper-surface discontinuities in the three spatial coordinates - we will assume that our representation has directional sensitivity with respect to the 3 spatial coordinates (but not along the time coordinate). One of the main results in this paper is that this new construction provides highly sparse representations for the class of 4-dimensional cylindrical cartoon-like functions - the simplified model we adopt for spatio-temporal data - outperforming more conventional representations. To further illustrate the superior approximation properties of cylindrical shearlets, we consider a problem of undersampled reconstruction in dynamic tomography using synthetic data that simulate a breathing chest.

Finally, we remark that shearlets have been already applied in (2d+1) video applications. For instance, conventional 3d-shearlets were employed in [17] to provide efficient video representations and, more recently, to detect relevant space-time features of videos in [18]. As we discuss below, the cylindrical shearlets we consider in this paper are derived from a modified construction that handles spatial and temporal coordinates with different geometric sensitivities. As already indicated by some of the authors in [19] and further argued in this paper, this construction entails distinct mathematical properties with respect to conventional shearlets and significant potential advantages in the context of spatio-temporal data.

### 1.1. Sparse 4-dimensional representations

To explain the significance of our new representation, we start with a heuristic argument showing why cylindrical shearlets are expected to be especially effective in representing a compactly supported piecewise regular function  $f$  of four variables with discontinuities in the first 3 spatial coordinates. To keep this explanation at an intuitive level, we will postpone the precise definition of the class  $\mathcal{E}(A)$  of cylindrical cartoon-like functions to Sec. 3.

We start by examining the *4d wavelet expansion* of  $f$  using a Parseval frame of wavelets  $\{\varphi_{j,k}(x) = 2^{4j}\varphi(2^{2j}x - k) : j \in \mathbb{Z}, k \in \mathbb{Z}^4\} \subset L^2(\mathbb{R}^4)$  where  $\varphi$  is well localized. We choose  $2^{2j}$  as dilation factor rather than  $2^j$  to be consistent with the cylindrical shearlet representation. An element  $\varphi_{j,k}$  of the wavelet system at scale of  $2^{-2j}$  is essentially supported on a box of size  $2^{-2j} \times 2^{-2j} \times 2^{-2j} \times 2^{-2j}$ . Since the surface of discontinuity of  $f$  has finite volume in the 4d-space, there are approximately  $2^{6j}$  wavelet coefficients  $F_{j,k}(f) = \langle f, \varphi_{j,k} \rangle$  associated with this surface, while the remaining coefficients are negligible at fine scales. A direct computation shows that

$$\int_{\mathbb{R}^4} |\varphi_{j,k}(x)| dx = 2^{4j} \int_{\mathbb{R}^4} |\varphi(2^{2j}x - k)| dx = 2^{-4j} \int_{\mathbb{R}^4} |\varphi(y)| dy \leq c 2^{-4j},$$

for a constant  $c > 0$ . Hence, at scale of  $2^{-2j}$ , we have

$$|F_{j,k}(f)| \leq \|f\|_{\infty} \|\varphi_{j,k}\|_{L^1} \leq c 2^{-4j}.$$

For brevity, here and in the following we use the convention that the same letter  $c$  or  $C$  may denote different uniform constants. Thus, letting  $N = 2^{6j}$ , the  $N$ -th largest wavelet coefficient of  $f$  in magnitude, denoted by  $|F(f)|_N$ , is bounded by  $O(N^{-\frac{2}{3}})$ . Hence, if  $f_N^{(wav)}$  is the approximation of  $f$  obtained by taking the  $N$  largest coefficients (in absolute value) of its wavelet expansion, we have

$$\|f - f_N^{(wav)}\|_{L^2}^2 \leq \sum_{\mu > N} |F(f)|_\mu^2 \leq c N^{-\frac{1}{3}}.$$

Next, we examine the  $4d$  cylindrical shearlet expansion of  $f$ . The elements of the cylindrical shearlet system  $\psi_{j,\ell,k}$  are essentially of the form  $2^{3j}\psi(A^j B_\ell x - k)$ , where  $\psi$  is a bounded well-localized function,  $A$  is a diagonal matrix with factors  $(2^{2j}, 2^j, 2^j, 2^{2j})$  and  $B_\ell$  is an appropriate shear matrix. As a result, a direct estimate shows that there is a constant  $c > 0$  such that

$$\int_{\mathbb{R}^4} |\psi_{j,k,\ell}(x)| dx = 2^{-3j} \int_{\mathbb{R}^4} |\psi(y)| dy \leq c 2^{-3j}.$$

Hence, at scale  $2^{-2j}$ , the cylindrical shearlet coefficients  $s_{j,k,\ell} = \langle f, \psi_{j,\ell,k} \rangle$  are bounded by

$$|s_{j,k,\ell}(f)| \leq \|f\|_\infty \|\psi_{j,k,\ell}\|_{L^1} \leq c 2^{-3j}.$$

Each element  $\psi_{j,\ell,k}$  is essentially supported on a parallelepiped of size  $2^{-2j} \times 2^{-j} \times 2^{-j} \times 2^{-2j}$  with various orientations controlled by  $\ell$  and, due to directional sensitivity and elongated support, the only significant cylindrical shearlet coefficients occur when an element  $\psi_{j,\ell,k}$  is tangent to the surface of discontinuity of  $f$ . Only about  $2^{3j}$  cylindrical shearlet coefficients are significant. Thus, letting  $N = 2^{3j}$ , the  $N$ -th largest cylindrical shearlet coefficient in absolute value, denoted as  $|s(f)|_N$ , is bounded by  $O(N^{-1})$ . If we denote as  $f_N^{(csh)}$  the approximation of  $f$  obtained by taking the  $N$  largest coefficients (in absolute value) of its shearlet expansion, we have

$$\|f - f_N^{(csh)}\|_{L^2}^2 \leq \sum_{\mu > N} |s(f)|_\mu^2 \leq c N^{-1}.$$

We will show below using a rigorous argument that the estimate above is essentially correct.

## 1.2. Outline

The rest of the paper is organized as follows. In Sec. 2, we introduce a new construction of 4-dimensional cylindrical shearlets by generalizing the 3-dimensional construction in [19]. In Sec. 3, we present our sparse approximation results using 4-dimensional cylindrical shearlets, whose proofs are postponed to Sec. 4. We present a numerical implementation of 4-dimensional cylindrical shearlets in Sec. 5 and apply this representation to a problem from dynamic tomography in Sec. 6. We finally provide concluding remarks in Sec. 7.

## 2. Cylindrical shearlets

Cylindrical shearlets were recently introduced by some of the authors [19] as a variant of the shearlet construction in the 3-dimensional setting. As indicated above, this construction is motivated by applications in the analysis of data where the main discontinuities are perpendicular to one of the coordinate axes so that it is useful to employ representations that are direction-sensitive with respect to one hyperspace.

In the 4-dimensional setting, we associate cylindrical shearlets to three cylindrical hyper-pyramids defined as:

$$\begin{aligned}\mathcal{P}_1 &= \{(\xi_1, \xi_2, \xi_3, \xi_4) \in \mathbb{R}^4 : |\frac{\xi_2}{\xi_1}| \leq 1, |\frac{\xi_3}{\xi_1}| \leq 1\}, \\ \mathcal{P}_2 &= \{(\xi_1, \xi_2, \xi_3, \xi_4) \in \mathbb{R}^4 : |\frac{\xi_1}{\xi_2}| \leq 1, |\frac{\xi_3}{\xi_2}| \leq 1\}, \\ \mathcal{P}_3 &= \{(\xi_1, \xi_2, \xi_3, \xi_4) \in \mathbb{R}^4 : |\frac{\xi_1}{\xi_3}| \leq 1, |\frac{\xi_2}{\xi_3}| \leq 1\}.\end{aligned}$$

**Definition 2.1.** For  $d = 1, 2, 3$ , a pyramid-based cylindrical shearlet system associated with the pyramid  $\mathcal{P}_d$  is a collection of functions

$$\{\psi_{j,\ell_1,\ell_2,k}^{(d)} : j \geq 0, |\ell_1|, |\ell_2| \leq 2^j, k \in \mathbb{Z}^4\}, \quad (1)$$

where the elements of the system (1) are given in the Fourier domain as

$$\hat{\psi}_{j,\ell,k}^{(d)}(\xi) = |\det A_{(d)}|^{-\frac{j}{2}} W(2^{-2j}\xi) V_{(d)}(\xi A_{(d)}^{-j} B_{(d)}^{[-\ell]}) e^{2\pi i \xi A_{(d)}^{-j} B_{(d)}^{[-\ell]} k} \quad (2)$$

with  $\ell = (\ell_1, \ell_2)$  and the matrices  $A_{(d)}$  and  $B_{(d)}^{[\ell]}$  given by

$$\begin{aligned}A_{(1)} &= \begin{pmatrix} 4 & 0 & 0 & 0 \\ 0 & 2 & 0 & 0 \\ 0 & 0 & 2 & 0 \\ 0 & 0 & 0 & 4 \end{pmatrix}, \quad A_{(2)} = \begin{pmatrix} 2 & 0 & 0 & 0 \\ 0 & 4 & 0 & 0 \\ 0 & 0 & 2 & 0 \\ 0 & 0 & 0 & 4 \end{pmatrix}, \quad A_{(3)} = \begin{pmatrix} 2 & 0 & 0 & 0 \\ 0 & 2 & 0 & 0 \\ 0 & 0 & 4 & 0 \\ 0 & 0 & 0 & 4 \end{pmatrix}, \\ B_{(1)}^{[\ell]} &= \begin{pmatrix} 1 & \ell_1 & \ell_2 & 0 \\ 0 & 1 & 0 & 0 \\ 0 & 0 & 1 & 0 \\ 0 & 0 & 0 & 1 \end{pmatrix}, \quad B_{(2)}^{[\ell]} = \begin{pmatrix} 1 & 0 & 0 & 0 \\ \ell_1 & 1 & \ell_2 & 0 \\ 0 & 0 & 1 & 0 \\ 0 & 0 & 0 & 1 \end{pmatrix}, \quad B_{(3)}^{[\ell]} = \begin{pmatrix} 1 & 0 & 0 & 0 \\ 0 & 1 & 0 & 0 \\ \ell_1 & \ell_2 & 1 & 0 \\ 0 & 0 & 0 & 1 \end{pmatrix}.\end{aligned}$$

As we show below, we can choose the functions  $W$  and  $V_{(d)}$  so that the corresponding system (1) is a smooth Parseval frame of  $L^2(\mathcal{P}_d \setminus C_0)^\vee$ , for  $d = 1, 2, 3$  where  $C_0 = [-\frac{1}{8}, \frac{1}{8}]^4$ , that is,

$$f = \sum_{j \geq 0} \sum_{|\ell_1|, |\ell_2| \leq 2^j} \sum_{k \in \mathbb{Z}^4} \langle f, \psi_{j,\ell,k}^{(d)} \rangle \psi_{j,\ell,k}^{(d)},$$

for all  $f$  in  $L^2$  whose Fourier support is contained in  $\mathcal{P}_d \setminus C_0$ ; convergence is understood in the  $L^2$  norm.

2.1. *Smooth Parseval frame of cylindrical shearlets on  $L^2(\mathbb{R}^4)$*

Our construction below adapts the main ideas from the standard shearlet construction [20] and extends the 3-dimensional cylindrical shearlet construction [19].

We let  $\phi \in L^2(\mathbb{R}^4)$  be such that  $\hat{\phi} \in C_c^\infty$  with  $0 \leq \hat{\phi} \leq 1$  and

$$\hat{\phi}(\xi) = 1 \text{ if } \xi \in [-\frac{1}{16}, \frac{1}{16}], \quad \hat{\phi}(\xi) = 0 \text{ if } \xi \in \mathbb{R} \setminus [-\frac{1}{8}, \frac{1}{8}]. \quad (3)$$

Letting  $\hat{\Phi}(\xi_1, \xi_2, \xi_3, \xi_4) = \hat{\phi}(\xi_1)\hat{\phi}(\xi_2)\hat{\phi}(\xi_3)\hat{\phi}(\xi_4)$ , we define the window function

$$W(\xi) = \sqrt{\hat{\Phi}^2(2^{-2}\xi) - \hat{\Phi}^2(\xi)}.$$

It follows that

$$\hat{\phi}^2(\xi) + \sum_{j \geq 0} W^2(2^{-2j}\xi) = 1 \text{ for } \xi \in \mathbb{R}^4.$$

We notice that the functions  $W_j^2 = W^2(2^{-2j}\cdot)$  are supported in the Cartesian coranae

$$C_j = [-2^{2j-1}, 2^{2j-1}]^4 \setminus [-2^{2j-4}, 2^{2j-4}]^4 \subset \mathbb{R}^4$$

and that, by adding them up for  $j \geq 0$ , we obtain a smooth tiling of the frequency plane:

$$\sum_{j \geq 0} W^2(2^{-2j}\xi) = 1 \text{ for } \xi \in \mathbb{R}^4 \setminus [-\frac{1}{8}, \frac{1}{8}]^4.$$

In addition, we let  $v \in C^\infty(\mathbb{R})$  be such that  $\text{supp}(v) \subset [-1, 1]$

$$|v(u-1)|^2 + |v(u)|^2 + |v(u+1)|^2 = 1 \text{ for } |u| \leq 1.$$

It is shown in [2] that there exist examples of functions  $W, v$  satisfying the properties described above.

For  $d = 1$ , observing that  $|\det A_{(1)}| = 2^6$ , that

$$(\xi_1, \xi_2, \xi_3, \xi_4) A_{(1)}^{-j} B_{(1)}^{[-\ell]} = (2^{-2j}\xi_1, -2^{-2j}\ell_1\xi_1 + 2^{-j}\xi_2, -2^{-2j}\ell_2\xi_1 + 2^{-j}\xi_3, 2^{-2j}\xi_4)$$

and setting  $V_{(1)} = v(\frac{\xi_2}{\xi_1})v(\frac{\xi_3}{\xi_1})$ , an element of the system (2) can be written as

$$\hat{\psi}_{j,\ell,k}^{(1)}(\xi) = 2^{-3j} W(2^{-2j}\xi) v(2^j \frac{\xi_2}{\xi_1} - \ell_1) v(2^j \frac{\xi_3}{\xi_1} - \ell_2) e^{2\pi i \xi A_{(1)}^{-j} B_{(1)}^{[-\ell]} k}, \quad (4)$$

showing that the Fourier support of  $\psi_{j,\ell,k}^{(1)}$  is contained inside the region

$$U_{j,\ell} = \{ \xi \in [-2^{2j-1}, 2^{2j-1}]^4 \setminus [-2^{2j-4}, 2^{2j-4}]^4 : |\frac{\xi_2}{\xi_1} - \ell_1 2^{-j}| \leq 2^{-j}, \\ |\frac{\xi_3}{\xi_1} - \ell_2 2^{-j}| \leq 2^{-j} \} \subset \mathbb{R}^4. \quad (5)$$

Similar to conventional 3-dimensional shearlets [20], we obtain a smooth Parseval frame of cylindrical shearlets for  $L^2(\mathbb{R}^4)$  using an appropriate combinations of the pyramid-based systems (1) together with an additional coarse

scale system. To ensure that all elements of this combined system are smooth and compactly supported in Fourier domain, we appropriately modify the elements of the shearlet system overlapping the boundaries of the regions  $\mathcal{P}_1$ ,  $\mathcal{P}_2$  and  $\mathcal{P}_3$ . Hence a *cylindrical shearlet system for  $L^2(\mathbb{R}^4)$*  is given by

$$\begin{aligned} \Psi = & \left\{ \tilde{\psi}_{-1,k} : k \in \mathbb{Z}^4 \right\} \cup \left\{ \tilde{\psi}_{j,\ell,k,d} : j \geq 0, |\ell_1| \leq 2^j, |\ell_2| < 2^j, k \in \mathbb{Z}^4, d = 1, 2, 3 \right\} \\ & \cup \left\{ \tilde{\psi}_{j,\ell,k} : j \geq 0, \ell_1 = \pm 2^j, \ell_2 = \pm 2^j, k \in \mathbb{Z}^4 \right\}, \end{aligned} \quad (6)$$

consisting of:

- the *coarse-scale cylindrical shearlets*  $\{\tilde{\psi}_{-1,k} = \phi(\cdot - k) : k \in \mathbb{Z}^4\}$ , where  $\phi$  is given by (3);
- the *interior cylindrical shearlets*  $\{\tilde{\psi}_{j,\ell,k,d} = \psi_{j,\ell,k}^{(d)} : j \geq 0, |\ell_1| < 2^j, |\ell_2| < 2^j, k \in \mathbb{Z}^4, d = 1, 2, 3\}$ , with the functions  $\psi_{j,\ell,k}^{(d)}$  given by (1);
- the *boundary cylindrical shearlets*  $\{\tilde{\psi}_{j,\ell,k,d} : j \geq 0, \ell_1 = \pm 2^j, |\ell_2| < 2^j, k \in \mathbb{Z}^4, d = 1, 2, 3\}$  and  $\{\tilde{\psi}_{j,\ell,k} : j \geq 0, \ell_1, \ell_2 = \pm 2^j, k \in \mathbb{Z}^4\}$ , obtained by joining together slightly modified versions of  $\psi_{j,\ell,k}^{(d)}$  and  $\psi_{j,\ell,k}^{(d')}$ ,  $d \neq d'$ , for  $\ell_1, \ell_2 = \pm 2^j$ , after that they have been restricted in the Fourier domain to their cones  $\mathcal{P}_d, \mathcal{P}_{d'}$ , respectively. Their precise definition is very similar to [20, Sec. 3.1].

We remark that, by construction, the boundary shearlets  $\{\tilde{\psi}_{j,\ell,k} : j \geq 0, \ell_1, \ell_2 = \pm 2^j, k \in \mathbb{Z}^3\}$  are compactly supported in Fourier domain. In addition, we can show that they are smooth in Fourier domain using essentially the same argument as [20, Sec. 3.1].

For  $j \geq 1$ ,  $\ell = (\ell_1, \ell_2)$ ,  $\ell_1 = \pm 2^j$ ,  $|\ell_2| < 2^j$  we define

$$\begin{aligned} (\tilde{\psi}_{j,\ell,k,1})^\wedge(\xi) &= \begin{cases} 2^{-3j-4} W(2^{-2j}\xi) v(2^j \frac{\xi_2}{\xi_1} - \ell_1) v(2^j \frac{\xi_3}{\xi_1} - \ell_2) E_1(\xi) & \text{if } \xi \in \mathcal{P}_1 \\ 2^{-3j-4} W(2^{-2j}\xi) v(2^j \frac{\xi_1}{\xi_2} - \ell_1) v(2^j \frac{\xi_3}{\xi_2} - \ell_2) E_1(\xi) & \text{if } \xi \in \mathcal{P}_2 \end{cases} \\ (\tilde{\psi}_{j,\ell,k,2})^\wedge(\xi) &= \begin{cases} 2^{-3j-4} W(2^{-2j}\xi) v(2^j \frac{\xi_1}{\xi_2} - \ell_1) v(2^j \frac{\xi_3}{\xi_2} - \ell_2) E_2(\xi) & \text{if } \xi \in \mathcal{P}_2 \\ 2^{-3j-4} W(2^{-2j}\xi) v(2^j \frac{\xi_1}{\xi_3} - \ell_1) v(2^j \frac{\xi_2}{\xi_3} - \ell_2) E_2(\xi) & \text{if } \xi \in \mathcal{P}_3 \end{cases} \\ (\tilde{\psi}_{j,\ell,k,3})^\wedge(\xi) &= \begin{cases} 2^{-3j-4} W(2^{-2j}\xi) v(2^j \frac{\xi_2}{\xi_1} - \ell_2) v(2^j \frac{\xi_3}{\xi_1} - \ell_1) E_3(\xi) & \text{if } \xi \in \mathcal{P}_1 \\ 2^{-3j-4} W(2^{-2j}\xi) v(2^j \frac{\xi_1}{\xi_3} - \ell_1) v(2^j \frac{\xi_2}{\xi_3} - \ell_2) E_3(\xi) & \text{if } \xi \in \mathcal{P}_3 \end{cases} \end{aligned}$$

where  $E_d(\xi) = e^{2\pi i \xi 2^{-2} A_{(d)}^{-j} B_{(d)}^{[-(\ell_1, \ell_2)]} k}$ , for  $d = 1, 2, 3$ .

Similarly, for  $j \geq 1$ ,  $\ell_1, \ell_2 = \pm 2^j$  we define

$$(\tilde{\psi}_{j,\ell,k})^\wedge(\xi) = \begin{cases} 2^{-3j-4} W(2^{-2j}\xi) v(2^j \frac{\xi_2}{\xi_1} - \ell_1) v(2^j \frac{\xi_3}{\xi_1} - \ell_2) E_1(\xi) & \text{if } \xi \in \mathcal{P}_1 \\ 2^{-3j-4} W(2^{-2j}\xi) v(2^j \frac{\xi_1}{\xi_2} - \ell_1) v(2^j \frac{\xi_3}{\xi_2} - \ell_2) E_1(\xi) & \text{if } \xi \in \mathcal{P}_2 \\ 2^{-3j-4} W(2^{-2j}\xi) v(2^j \frac{\xi_1}{\xi_3} - \ell_1) v(2^j \frac{\xi_2}{\xi_3} - \ell_2) E_1(\xi) & \text{if } \xi \in \mathcal{P}_3. \end{cases}$$

For  $j = 0$ ,  $\ell_1 = \pm 1$ , we define

$$\begin{aligned} (\tilde{\psi}_{0,\ell_1,0,k,1})^\wedge(\xi) &= \begin{cases} W(\xi) v(\frac{\xi_2}{\xi_1} - \ell_1) v(\frac{\xi_3}{\xi_1}) e^{2\pi i \xi k} & \text{if } \xi \in \mathcal{P}_1 \\ W(\xi) v(\frac{\xi_1}{\xi_2} - \ell_1) v(\frac{\xi_3}{\xi_2}) e^{2\pi i \xi k} & \text{if } \xi \in \mathcal{P}_2 \end{cases} \\ (\tilde{\psi}_{0,\ell_1,0,k,2})^\wedge(\xi) &= \begin{cases} W(\xi) v(\frac{\xi_1}{\xi_2}) v(\frac{\xi_3}{\xi_2} - \ell_1) e^{2\pi i \xi k} & \text{if } \xi \in \mathcal{P}_2 \\ W(\xi) v(\frac{\xi_1}{\xi_3}) v(\frac{\xi_2}{\xi_3} - \ell_1) e^{2\pi i \xi k} & \text{if } \xi \in \mathcal{P}_3 \end{cases} \\ (\tilde{\psi}_{0,\ell_1,0,k,3})^\wedge(\xi) &= \begin{cases} W(\xi) v(\frac{\xi_2}{\xi_1}) v(\frac{\xi_3}{\xi_1} - \ell_1) e^{2\pi i \xi k} & \text{if } \xi \in \mathcal{P}_1 \\ W(\xi) v(\frac{\xi_1}{\xi_3} - \ell_1) v(\frac{\xi_2}{\xi_3}) e^{2\pi i \xi k} & \text{if } \xi \in \mathcal{P}_3. \end{cases} \end{aligned}$$

For  $j = 0$ ,  $\ell_1, \ell_2 = \pm 1$ , we define

$$(\tilde{\psi}_{0,\ell_1,\ell_2,k})^\wedge(\xi) = \begin{cases} W(\xi) v(\frac{\xi_2}{\xi_1} - \ell_1) v(\frac{\xi_3}{\xi_1} - \ell_2) e^{2\pi i \xi k} & \text{if } \xi \in \mathcal{P}_1 \\ W(\xi) v(\frac{\xi_1}{\xi_2} - \ell_1) v(\frac{\xi_3}{\xi_2} - \ell_2) e^{2\pi i \xi k} & \text{if } \xi \in \mathcal{P}_2 \\ W(\xi) v(\frac{\xi_1}{\xi_3} - \ell_1) v(\frac{\xi_2}{\xi_3} - \ell_2) e^{2\pi i \xi k} & \text{if } \xi \in \mathcal{P}_3 \end{cases}$$

We have the following result whose proof is similar to [20].

**Theorem 2.2.** *The shearlet system  $\Psi \subset L^2(\mathbb{R}^4)$ , given by (6), is a Parseval frame for  $L^2(\mathbb{R}^4)$ . Furthermore, the elements of this system are  $C^\infty$  and compactly supported in the Fourier domain.*

For simplicity, in the following we will denote the cylindrical system of shearlets in (6) as

$$\Psi = \{\tilde{\psi}_\mu : \mu \in M\}, \quad (7)$$

where  $M = M_C \cup M_I \cup M_B$  are the indices associated with

- $M_C = \{(j, k) : j = -1, k \in \mathbb{Z}^4\}$  coarse-scale shearlets,
- $M_I = \{(j, \ell_1, \ell_2, k, d) : j \geq 0, |\ell_1| < 2^j, |\ell_2| < 2^j, k \in \mathbb{Z}^4, d = 1, 2, 3\}$  interior shearlets,
- $M_B = \{(j, \ell_1, \ell_2, k, d) : j \geq 0, |\ell_1| = \pm 2^j, |\ell_2| < 2^j, k \in \mathbb{Z}^4, d = 1, 2, 3\} \cup \{(j, \ell_1, \ell_2) : j \geq 0, \ell_1, \ell_2 = \pm 2^j, k \in \mathbb{Z}^4\}$  boundary shearlets.

For  $f \in L^2(\mathbb{R}^4)$ , the *cylindrical shearlet transform*  $\mathcal{S}$  is the mapping

$$f \mapsto \mathcal{S}(f) = \langle f, \tilde{\psi}_\mu \rangle, \quad \mu \in M.$$

We remark that, by a direct computation, we can write the shearlet functions in (1) as

$$\psi_{j,\ell_1,\ell_2,k}^{(d)}(x) = |\det A_{(d)}|^{j/2} \psi_{j,\ell_1,\ell_2}^{(d)} \left( B_{(d)}^{[\ell]} A_{(d)}^j x + k \right) \quad (8)$$

where  $\hat{\psi}_{j,\ell_1,\ell_2}^{(d)}(\xi) = W \left( 2^{-2j} \xi B_{(d)}^{[\ell]} A_{(d)}^j \right) V_{(d)}(\xi)$  depends mildly on  $j, \ell_1, \ell_2$ . Using the support and regularity of  $W$  and  $V$ , a calculation similar to [20] shows that for any  $\nu \in (\mathbb{N} \cup \{0\})^4$  and any  $N > 0$ , there is  $C_{\nu,N} > 0$  independent of  $j, \ell_1, \ell_2, d$  such that

$$\partial_x^\nu \psi_{j,\ell_1,\ell_2}^{(d)}(x) \leq C_{\nu,N} (1 + |x|)^{-N}. \quad (9)$$

### 3. Sparse cylindrical shearlets approximations

We start by defining the class of 4-dimensional cylindrical cartoon-like functions associated with our data model. This definition extends a similar definition in the 3-dimensional setting that was introduced by some of the authors [19] as a modification of the better known class of *cartoon-like functions*, originally proposed by Donoho [21] to provide a simplified model of natural images.

#### 3.1. Cylindrical cartoon-like functions

For a fixed constant  $A > 0$ , let  $\mathcal{M}(A)$  be a class of indicator functions of sets  $B \subset [0, 1]^3$  with  $C^2$ -regular 2-manifold boundary  $\partial B = \bigcup_{\alpha} \Sigma_{\alpha}$ . Here  $\alpha$  ranges over a finite index set and  $\Sigma_{\alpha} = \{(v, E_{\alpha}(v)) : v \in V_{\alpha} \subset \mathbb{R}^2\}$  such that  $\|E_{\alpha}\|_{C^2(V_{\alpha})} \leq A$  for all  $\alpha$ . Denoting with  $C^2([0, 1]^3)$  the collection of twice differentiable functions supported inside  $[0, 1]^3$ , we define the class of 4-dimensional cylindrical cartoon-like functions  $\mathcal{E}(A)$  as the set

$$\{f = h_0 g_0 + h_1 \mathcal{X}_B g_1 : \mathcal{X}_B \in \mathcal{M}(A), h_0, h_1 \in C^2([0, 1]^3), g_0, g_1 \in C^2([-1, 1])\}$$

where

$$f(x_1, x_2, x_3, x_4) = h_0(x_1, x_2, x_3)g_0(x_4) + h_1(x_1, x_2, x_3)\mathcal{X}_B(x_1, x_2, x_3)g_1(x_4) \quad (10)$$

and  $\|f\|_{C^2} = \sum_{|\alpha| \leq 2} \|D^{\alpha} f\|_{\infty} \leq 1$ .

#### 3.2. Approximation theorems

Let  $\{\tilde{\psi}_{\mu}\}_{\mu \in M}$  be the Parseval frame of cylindrical shearlets given by (7). The cylindrical shearlet coefficients of  $f \in L^2(\mathbb{R}^4)$  are the elements of the sequence  $\{s_{\mu}(f) = \langle f, \tilde{\psi}_{\mu} \rangle : \mu \in M\}$ . We denote by  $|s(f)|_{(N)}$  the  $N$ -th largest entry in modulus of this sequence.

Here is the main result which will be proved in the next section.

**Theorem 3.1.** *Let  $f \in \mathcal{E}(A)$  and  $\{s_{\mu}(f) = \langle f, \tilde{\psi}_{\mu} \rangle : \mu \in M\}$  be the sequence of corresponding cylindrical shearlet coefficients. Then, for any  $N \in \mathbb{N}$ , there is a constant  $C$  independent of  $\mu$  and  $N$  such that*

$$\sup_{f \in \mathcal{E}(A)} |s_{\mu}(f)|_{(N)} \leq CN^{-1}(\log N). \quad (11)$$

Let  $f_N^S$  be the  $N$ -th term approximate of  $f \in \mathcal{E}(A)$  obtained from the  $N$ -th largest coefficients of its cylindrical shearlet expansion, namely  $f_N^S = \sum_{\mu \in I_N} \langle f, \tilde{\psi}_{\mu} \rangle \tilde{\psi}_{\mu}$  where  $I_N \subset M$  is the set of indices corresponding to the  $N$ -th largest entries of the sequence  $\{|\langle f, \tilde{\psi}_{\mu} \rangle|^2 : \mu \in M\}$ . The approximation error satisfies the estimate:

$$\|f - f_N^S\|_{L^2}^2 \leq \sum_{m > N} |s(f)|_{(m)}^2.$$

Thus, from Theorem 3.1 it follows directly the following result.

**Theorem 3.2.** *Let  $f \in \mathcal{E}(A)$  and  $f_N^S$  be the  $N$ -th term approximation defined above. Then, for  $N \in \mathbb{N}$ , there is a constant  $C$  independent of  $N$  and  $\mu$  such that*

$$\|f - f_N^S\|_{L^2}^2 \leq CN^{-1}(\log N)^2.$$

The decay estimate above is the same as the one found for 3-dimensional shearlets [22] which is the optimal rate in the class of 3-dimensional cartoon-like functions [22, 23] and is faster than the optimal decay rate  $O(N^{-2/3})$  valid for the class of 4-dimensional cartoon-like functions (cf.[23]). We conjecture that  $O(N^{-1})$  is indeed the optimal decay rate in the class of 4-dimensional cylindrical cartoon-like images.

### 3.3. Arguments and constructions

The general structure of the proof of Theorem 3.1 follows the structure of [22]. However, to deal with specific geometry of 4d cylindrical shearlets, we need to introduce some new technical constructions and modify some critical steps of the original arguments, especially in the proofs of Theorems. 3.3, 3.4 and 4.3 below.

Similar to [2, 22], we introduce the weak- $\ell^p$  quasi-norm  $\|\cdot\|_{w\ell^p}$  to measure the sparsity of the shearlet coefficients. For a sequence  $s = (s_\mu)_{\mu \in M}$ , this is defined as

$$\|s\|_{w\ell^p} = \sup_{N>0} N^{1/p} |s_\mu|_{(N)}$$

where  $|s_\mu|_{(N)}$  is the  $N$ -th largest entry in the sequence  $s$ . In [24], this norm is shown to be equivalent to

$$\|s\|_{w\ell^p} = \left( \sup_{\epsilon>0} \#\{\mu : |s_\mu| > \epsilon\} \epsilon^p \right)^{1/p}.$$

We intend to analyze the decay properties of the cylindrical shearlet coefficients  $\{\langle f, \tilde{\psi}_\mu \rangle : \mu \in M\}$ , where  $f$  is chosen according to our cylindrical cartoon-like model (10), that is,

$$f(x_1, x_2, x_3, x_4) = h(x_1, x_2, x_3) \mathcal{X}_B(x_1, x_2, x_3) g(x_4),$$

where  $\mathcal{X}_B \in \mathcal{M}(A)$ ,  $h \in C^2([0, 1]^3)$ ,  $g \in C^2([0, 1])$ .

We recall that *discontinuities only occur in the  $x_1 x_2 x_3$  space*. Thus, to carry out our analysis, we smoothly localize the function  $f$  near dyadic squares in the  $x_1 x_2 x_3$  space as follows. For a scale parameter  $j \geq 0$  fixed, we let

$$\mathcal{Q}_j = \left\{ Q = \left[ \frac{k_1}{2^j}, \frac{k_1+1}{2^j} \right] \times \left[ \frac{k_2}{2^j}, \frac{k_2+1}{2^j} \right] \times \left[ \frac{k_3}{2^j}, \frac{k_3+1}{2^j} \right] : k_1, k_2, k_3 \in \mathbb{Z} \right\}$$

be the collection of dyadic cubes. For a non-negative  $C^\infty$  function with support  $w$  in  $[-1, 1]^3$  we define a smooth partition of unity

$$\sum_{Q \in \mathcal{Q}_j} w_Q(x) = 1, \quad x \in \mathbb{R}^3,$$

where for each dyadic cube  $Q \in \mathcal{Q}_j$ ,  $w_Q(x) = w(2^j x - k)$  and  $k \in \mathbb{Z}^3$ . We will examine the cylindrical shearlet coefficients of  $f_Q := fw_Q$ , i.e.,  $\{\langle f_Q, \tilde{\psi}_\mu \rangle : \mu \in M_j\}$ , where  $M_j = \{\mu \in M : j \text{ is fixed}\}$ . As we show below, these coefficients exhibit a different decay behaviour depending on whether the surface  $\partial B$  intersects the support of  $w_Q$  or not. Let  $\mathcal{Q}_j = \mathcal{Q}_j^0 \cup \mathcal{Q}_j^1$  be the disjoint union of  $\mathcal{Q}_j^0 = \{Q \in \mathcal{Q}_j : \partial B \cap \text{supp}(w_Q) \neq \emptyset\}$  and  $\mathcal{Q}_j^1 = \{Q \in \mathcal{Q}_j : \partial B \cap \text{supp}(w_Q) = \emptyset\}$ . Notice each  $Q$  has side-length  $3 \cdot 2^{-j}$ , then  $|\mathcal{Q}_j^0| \lesssim 2^{2j}$ . Similarly, since  $\text{supp}(f) \subset [0, 1]^4$ , then  $\mathcal{Q}_j^1 \lesssim 2^{3j}$ . With this notation, we now state two theorems that will be used to prove Theorem 3.1. Note that while the decay rate in Theorem 3.3 is the same as in the one found for 3-dimensional shearlets in [22], the decay rate in Theorem 3.4 is different.

**Theorem 3.3.** *Let  $f \in \mathcal{E}(A)$ . For  $Q \in \mathcal{Q}_j^0$ , with  $j \geq 0$  fixed, the cylindrical shearlet coefficients  $\{\langle f_Q, \tilde{\psi}_\mu \rangle : \mu \in M_j\}$  satisfy*

$$\|\langle f_Q, \tilde{\psi}_\mu \rangle\|_{w\ell^1} \leq C2^{-2j},$$

where  $C$  is a constant independent of  $Q$  and  $j$ .

**Theorem 3.4.** *Let  $f \in \mathcal{E}(A)$ . For  $Q \in \mathcal{Q}_j^1$ , with  $j \geq 0$  fixed, the cylindrical shearlet coefficients  $\{\langle f_Q, \tilde{\psi}_\mu \rangle : \mu \in M_j\}$  satisfy*

$$\|\langle f_Q, \tilde{\psi}_\mu \rangle\|_{w\ell^1} \leq C2^{-7j/2},$$

where  $C$  is a constant independent of  $Q$  and  $j$ .

Before proving the theorems above, we show how these results are used to prove Theorem 3.1 using an argument very similar to [22]. First, we have the following corollary.

**Corollary 3.5.** *Let  $f \in \mathcal{E}(A)$  and for  $j \geq 0$ , consider the sequence of cylindrical shearlets coefficients  $s_j(f) = \{\langle f, \tilde{\psi}_\mu \rangle : \mu \in M_j\}$ . Then there is a constant  $C$  independent of  $j$  such that*

$$\|s_j(f)\|_{w\ell^1} \leq C.$$

**Proof.** Using Theorems 3.3, 3.4 and the triangle inequality for weak  $\ell^1$  spaces, we have

$$\begin{aligned} \|s_j(f)\|_{w\ell^1} &\leq \sum_{Q \in \mathcal{Q}_j} \|\langle f_Q, \tilde{\psi}_\mu \rangle\|_{w\ell^1} \\ &\leq \sum_{Q \in \mathcal{Q}_j^0} \|\langle f_Q, \tilde{\psi}_\mu \rangle\|_{w\ell^1} + \sum_{Q \in \mathcal{Q}_j^1} \|\langle f_Q, \tilde{\psi}_\mu \rangle\|_{w\ell^1} \\ &\leq C|\mathcal{Q}_j^0|2^{-2j} + C|\mathcal{Q}_j^1|2^{-7j/2} \\ &\leq C(2^{2j}2^{-2j} + 2^{3j}2^{-7j/2}) \leq C. \end{aligned}$$

In the last step, we have used the observations that  $|\mathcal{Q}_j^0| \leq C2^{2j}$  and  $|\mathcal{Q}_j^1| \leq C2^{3j}$ .  $\square$

We next prove Theorem 3.1.

**Proof of Theorem 3.1.** By Corollary 3.5, we have that

$$R(j, \epsilon) = \#\{\mu \in M_j : |\langle f, \tilde{\psi}_\mu \rangle| > \epsilon\} \leq C\epsilon^{-1} \quad (12)$$

For an interior shearlet  $\psi_{j,\ell,k}^{(d)}$ , given by (2), a direct computation using (8) and (9) gives that

$$\begin{aligned} |\langle f, \psi_{j,\ell,k}^{(d)} \rangle| &= \left| \int_{\mathbb{R}^4} f(x) |\det A_{(d)}|^{j/2} \psi_{j,\ell}^{(d)} \left( B_{(d)}^{[\ell]} A_{(d)}^j x + k \right) dx \right| \\ &\leq 2^{3j} \|f\|_\infty \int_{\mathbb{R}^4} |\psi_{j,\ell}^{(d)} \left( B_{(d)}^{[\ell]} A_{(d)}^j x + k \right)| dx \\ &\leq 2^{-3j} \|f\|_\infty \int_{\mathbb{R}^4} |\psi_{j,\ell}^{(d)}(y)| dy \\ &\leq C2^{-3j}. \end{aligned} \quad (13)$$

A very similar computation on the boundary shearlets gives the same estimate. So, for a given  $\epsilon > 0$ , there is  $j_\epsilon > 0$  such that  $|\langle f, \tilde{\psi}_{\mu(j)} \rangle| < \epsilon$  for each  $j \geq j_\epsilon$ . Therefore, from (13), we have  $R(j, \epsilon) = 0$  for  $j > \frac{1}{3} \log_2(\epsilon^{-1}) + \log_2(C) > \frac{1}{3} \log_2(\epsilon^{-1})$ . So, using (12), we have

$$\#\{\mu \in M : |\langle f, \tilde{\psi}_\mu \rangle| > \epsilon\} \leq \sum_{j \geq 0} R(j, \epsilon) = \sum_{j=0}^{\frac{1}{3} \log_2(\epsilon^{-1})} R(j, \epsilon) \leq C\epsilon^{-1} \log_2(\epsilon^{-1}).$$

Next, let  $n = n(\epsilon) = \#\{\mu \in M : |\langle f, \tilde{\psi}_\mu \rangle| > \epsilon\}$ . Notice  $\epsilon^{-1} \lesssim n$ . Therefore, from (3.3), we have  $\epsilon \leq Cn^{-1} \log_2(\epsilon^{-1}) \leq Cn^{-1} \log_2(n)$ . So, if  $|s(f)|_{(N)}$  is the  $N$ -th largest coefficient, then  $|s(f)|_{(N)} \leq CN^{-1} \log_2(N)$  and inequality (11) follows.  $\square$

#### 4. Proofs of Theorems 3.3 and 3.4

Here we assume the notation introduced above where  $f_Q = f w_Q$ , for  $f \in \mathcal{E}(A)$ . We remark that the localization window  $w_Q$  acts in the  $x_1 x_2 x_3$  space. Below, we will select  $w_Q$  appropriately so that we can analyze the discontinuity surface  $\partial B$  locally.

By choosing  $j > j_0$  sufficiently large, the scale  $2^{-j}$  is small enough so that, over a cube  $Q$  of side  $2^{-j}$ , the surface  $\partial B$  may be parametrized as  $x_1 = E(x_2, x_3)$  or  $x_2 = E(x_1, x_3)$  or  $x_3 = E(x_1, x_2)$ . For simplicity, we assume this surface satisfies

$$x_1 = E(x_2, x_3), \quad |x_2|, |x_3| \leq 2^{-j},$$

as the other cases can be analyzed with a very similar argument. By a suitable translation, we may assume that the surface contains the origin, that is  $k = (0, 0, 0)$ , and the normal direction of the surface at  $(0, 0, 0)$  is  $(1, 0, 0)$ . This is equivalent to assuming that  $E(0, 0) = E_{x_2}(0, 0) = E_{x_3}(0, 0) = 0$ . There is

no loss in generality in analyzing only this case since the situation where the surface does not contain the origin or has a different normal direction can be easily converted into this case by translation and rotation. So, the function  $f_Q$  is localized on  $Q = [0, 2^{-j}]^3$ . To simplify notation, for a function  $g(x)$  with  $x \in \mathbb{R}^2$  and  $m = (m_1, m_2)$  with  $0 \leq |m| = m_1 + m_2 \leq 2$ , we will write  $\frac{\partial^m}{\partial x^m} g$  as  $g_m$ .

The Taylor expansion of  $E$  around  $(0, 0)$  is  $E(x_2, x_3) = \frac{1}{2}(E_{(2,0)}(c)x_2^2 + 2E_{(1,1)}(c)x_2x_3 + E_{(0,2)}(c)x_3^2)$  where  $c = (c_2, c_3) \in [-2^{-j}, 2^{-j}]^2$ . Therefore, for  $j > j_0$  we have

$$|E(x_2, x_3)| \leq 2^{-2j}(\|E_{(2,0)}\|_\infty + \|E_{(1,1)}\|_\infty + \|E_{(0,2)}\|_\infty).$$

We will discuss the case  $j \leq j_0$  further below.

Recall that  $f$  has the form  $f(x_1, x_2, x_3, x_4) = h(x_1, x_2, x_3)\mathcal{X}_B(x_1, x_2, x_3)g(x_4)$  and we want to estimate the decay of  $f$  near the surface of discontinuity. Hence, for  $j \in \mathbb{Z}$ , we define the **surface fragment** as the function

$$h_Q(x_1, x_2, x_3) = w(2^j x)h(x_1, x_2, x_3)\mathcal{X}_{\{x_1 > E(x_2, x_3)\}}(x_1, x_2, x_3) \quad (14)$$

where  $w \in C^\infty([-1, 1]^3)$  is a non-negative window function. That is,  $w(2^j \cdot)$  is the window function  $w_Q$  announced above.

Note that  $h \in C^2([0, 1]^3)$ , hence  $h_Q$  is supported on  $[0, 2^{-j}]^3$ . Consequently, we define the localized version of  $f$  as  $f_Q(x_1, x_2, x_3, x_4) = h_Q(x_1, x_2, x_3)g(x_4)$ .

#### 4.1. Analysis of the Surface Fragment

We aim at deriving  $L^2$  estimates for the elements of the Parseval frame of cylindrical shearlets against  $f_Q = h_Q g$ , where  $h_Q$  is the the surface fragment (14). For our analysis below, it will be sufficient to consider the interior cylindrical shearlets (4) associated with the pyramidal region  $\mathcal{P}_1$ . Boundary shearlets and interior shearlets in the regions  $\mathcal{P}_2$  and  $\mathcal{P}_3$  satisfy similar support and regularity conditions, so that the corresponding estimates against  $f_Q$  are very similar.

In the following, we will express the first three coordinates of  $\xi \in \mathbb{R}^4$  in spherical coordinates, so we write  $(\xi_1, \xi_2, \xi_3) = (\rho \cos \theta \sin \phi, \rho \sin \theta \sin \phi, \rho \cos \phi)$  where  $\rho > 0$ ,  $\theta \in [0, 2\pi)$  and  $\phi \in [0, \pi]$ . Since we only consider the region  $\mathcal{P}_1$ , we can assume that  $\phi \in [\frac{\pi}{4}, \frac{3\pi}{4}]$   $\theta \in [-\frac{\pi}{4}, \frac{\pi}{4}]$ . We additionally remark that the variables  $\xi_2$  and  $\xi_3$  are symmetric in  $\mathcal{P}_1$ ; thus, we may assume that  $|\ell_1| \leq |\ell_2|$ .

For  $\xi \in \mathcal{P}_1 \subset \mathbb{R}^4$ ,  $j \geq 0$ ,  $|\ell_1| \leq |\ell_2| \leq 2^j$ , we let

$$\Gamma_{j,\ell}(\xi) = W(2^{-2j}\xi) v(2^j \frac{\xi_2}{\xi_1} - \ell_1) v(2^j \frac{\xi_3}{\xi_1} - \ell_2). \quad (15)$$

Using this notation, the interior shearlets (2) associated with the pyramidal region  $\mathcal{P}_1$  may be written as

$$\hat{\psi}_{j,\ell,k}^{(1)}(\xi) = 2^{-3j} \Gamma_{j,\ell}(\xi) e^{2\pi i \xi A_{(1)}^{-j} B_{(1)}^{[-\ell]} k}.$$

We consider the multi-index  $m = (m_1, m_2, m_3, m_4) \in \mathbb{N}^4$  with  $|m| = m_1 + m_2 + m_3 + m_4$  and write  $x^m = x_1^{m_1} x_2^{m_2} x_3^{m_3} x_4^{m_4}$  and  $\frac{\partial^m}{\partial \xi^m} \hat{f} = \frac{\partial^{m_1}}{\partial \xi_1^{m_1}} \frac{\partial^{m_2}}{\partial \xi_2^{m_2}} \frac{\partial^{m_3}}{\partial \xi_3^{m_3}} \frac{\partial^{m_4}}{\partial \xi_4^{m_4}} \hat{f}$ .

We have the following useful Lemma whose proof is similar to Sec.4.3 in [22].

**Lemma 4.1.** *Let  $h_Q$  be the surface fragment defined by (14) and  $\hat{h}_Q$  be the corresponding Fourier transform. Let*

$$(\xi_1, \xi_2, \xi_3) = (r \sin \theta' \cos \phi', -r \cos \theta', -r \sin \theta' \sin \phi') \subset \mathcal{P}_1$$

(which implies  $|\phi'| \leq \pi/4$ ). We then have the following estimates.

(a) *If the support of  $h_Q$  does not intersect the surface  $\partial B$ , then*

$$\int_{2^{2j-4}}^{2^{j+1}} \int_0^{2\pi} \left| \frac{\partial^{m_1}}{\partial \xi_1^{m_1}} \frac{\partial^{m_2}}{\partial \xi_2^{m_2}} \frac{\partial^{m_3}}{\partial \xi_3^{m_3}} \hat{h}_Q(r, \theta', \phi') \right|^2 d\theta' dr \leq C 2^{-2jm_1} 2^{-12j}.$$

(b) *If  $h_Q$  intersects the surface  $\partial B$  and  $|\sin \phi'| \leq 2^{1-j}$ , then*

$$\int_{2^{2j-4}}^{2^{j+1}} \int_0^{2\pi} \left| \frac{\partial^{m_1}}{\partial \xi_1^{m_1}} \frac{\partial^{m_2}}{\partial \xi_2^{m_2}} \frac{\partial^{m_3}}{\partial \xi_3^{m_3}} \hat{h}_Q(r, \theta', \phi') \right|^2 d\theta' dr \leq C 2^{-2jm_1} 2^{-7j}$$

(c) *If  $h_Q$  intersects the surface  $\partial B$  and  $|\sin \phi'| \geq 2^{1-j}$ , then*

$$\int_{2^{2j-4}}^{2^{j+1}} \int_0^{2\pi} \left| \frac{\partial^{m_1}}{\partial \xi_1^{m_1}} \frac{\partial^{m_2}}{\partial \xi_2^{m_2}} \frac{\partial^{m_3}}{\partial \xi_3^{m_3}} \hat{h}_Q(r, \theta', \phi') \right|^2 d\theta' dr \leq C 2^{-2jm_1} 2^{-12j} |\sin \phi'|^{-5}.$$

Note that, in the above lemma, the notation

$$\frac{\partial^{m_1}}{\partial \xi_1^{m_1}} \frac{\partial^{m_2}}{\partial \xi_2^{m_2}} \frac{\partial^{m_3}}{\partial \xi_3^{m_3}} \hat{h}_Q(r, \theta', \phi')$$

means that we first compute  $\frac{\partial^{m_1}}{\partial \xi_1^{m_1}} \frac{\partial^{m_2}}{\partial \xi_2^{m_2}} \frac{\partial^{m_3}}{\partial \xi_3^{m_3}} \hat{h}_Q(\xi_1, \xi_2, \xi_3)$  and next we make the change of variable  $(\xi_1, \xi_2, \xi_3) = (r \sin \theta' \cos \phi', -r \cos \theta', -r \sin \theta' \sin \phi')$ .

We also have the following Lemma whose proof is similar to [22, Lemma 2.5].

**Lemma 4.2.** *Let  $\Gamma_{j,\ell}$  be defined by (15). Then, for  $j \geq 1$ ,  $|\ell_1| \leq |\ell_2| \leq 2^j$  and  $m = (m_1, m_2, m_3, m_4) \in \mathbb{N}^4$  we have*

$$\left| \frac{\partial^{m_1}}{\partial \xi_1^{m_1}} \frac{\partial^{m_2}}{\partial \xi_2^{m_2}} \frac{\partial^{m_3}}{\partial \xi_3^{m_3}} \frac{\partial^{m_4}}{\partial \xi_4^{m_4}} \Gamma_{j,\ell}(\xi) \right| \leq C_m 2^{-m_1 j} 2^{-|m|j} (1 + |\ell_2|)^{m_1}.$$

Observing that the supports of  $\Gamma_{j,\ell_1,\ell_2}$  and  $|\Gamma_{j,\ell'_1,\ell_2}$  are disjoint provided that  $\ell_1 \neq \ell'_1$ , it follows from Lemma 4.2 that

$$\sum_{\ell_1 = -|\ell_2|}^{|\ell_2|} \left| \frac{\partial^{m_1}}{\partial \xi_1^{m_1}} \frac{\partial^{m_2}}{\partial \xi_2^{m_2}} \frac{\partial^{m_3}}{\partial \xi_3^{m_3}} \frac{\partial^{m_4}}{\partial \xi_4^{m_4}} \Gamma_{j,\ell}(\xi) \right| \leq C_m 2^{-m_1 j} 2^{-|m|j} (1 + |\ell_2|)^{m_1}.$$

We can now prove the following result.

**Theorem 4.3.** *Let  $f_Q = h_Q g$ , where  $h_Q$  is the surface fragment given by (14),  $g \in C^2([-1, 1])$  and  $\Gamma_{j,\ell}$  is given by (15). Let  $m_f = (m_{f_1}, m_{f_2}, m_{f_3}, m_{f_4})$  and  $m_\gamma = (m_{\gamma_1}, m_{\gamma_2}, m_{\gamma_3}, m_{\gamma_4})$  be multi-indexes. Then there exists a constant  $C$  independent of  $j, \ell$  such that*

$$\begin{aligned} & \sum_{\ell_1 = -|\ell_2|}^{|\ell_2|} \int_{\mathbb{R}^4} \left| \frac{\partial^{m_f}}{\partial \xi^{m_f}} \widehat{f}_Q(\xi) \right|^2 \left| \frac{\partial^{m_\gamma}}{\partial \xi^{m_\gamma}} \Gamma_{j,\ell}(\xi) \right|^2 d\xi \\ & \leq C 2^{-m_{\gamma_1} j} 2^{-|m_\gamma|j} (1 + |\ell_2|)^{m_{\gamma_1}} 2^{-2j m_{f_1}} (2^{-4j} (1 + |\ell_2|^{-5}) + 2^{-9j}). \end{aligned}$$

**Proof.** Recall that the support of  $\Gamma_{j,\ell}$  is contained in  $\mathcal{P}_1$  and depends on the supports of  $W$  and  $v$ . So, for  $\xi = (\xi_1, \xi_2, \xi_3, \xi_4) \in \text{supp } \Gamma_{j,\ell}$ , we have  $\xi_i \in [-2^{2j-1}, 2^{2j-1}] \setminus [-2^{2j-4}, 2^{2j-4}]$  for  $i = 1, 2, 3, 4$ ,  $|2^j \frac{\xi_2}{\xi_1} - \ell_1| \leq 1$  and  $|2^j \frac{\xi_3}{\xi_1} - \ell_2| \leq 1$ . By applying a change of variables into spherical coordinates, we can write  $(\xi_1, \xi_2, \xi_3) = (r \sin \theta' \cos \phi', -r \cos \theta', -r \sin \theta' \sin \phi')$ , where we have  $|-2^j \frac{\cot \theta'}{\cos \phi'} - \ell_1| \leq 1$  and  $|-2^j \tan \phi' - \ell_2| \leq 1$ . Thus,

$$r^2 = \xi_1^2 + \xi_2^2 + \xi_3^2 = \xi_1^2 \left( 1 + \left( \frac{\cot \theta'}{\cos \phi'} \right)^2 + (\tan \phi')^2 \right)$$

and  $2^{2j-4} \leq r \leq 2^{2j+2}$ . We also remark that  $|\phi'| \leq \pi/4$  since  $\Gamma_{j,\ell}$  is supported on  $\mathcal{P}_1$ . In addition, from  $(-1 - \ell_2)2^{-j} \leq \tan \phi' \leq (1 - \ell_2)2^{-j}$  and the Taylor expansion of the tangent function, we see that  $\phi'$  must be contained in an interval  $I_{\phi'}$  of length  $C2^{-j}$ . Hence, using Lemma 4.2 we have

$$\begin{aligned} & \sum_{\ell_1 = -|\ell_2|}^{|\ell_2|} \int_{\mathbb{R}^4} \left| \frac{\partial^{m_f}}{\partial \xi^{m_f}} \widehat{f}_Q(\xi) \right|^2 \left| \frac{\partial^{m_\gamma}}{\partial \xi^{m_\gamma}} \Gamma_{j,\ell}(\xi) \right|^2 d\xi \\ & \leq C_{m_\gamma} 2^{-m_{\gamma_1} j} 2^{-|m_\gamma|j} (1 + \ell_2)^{m_{\gamma_1}} \int_{\mathbb{R}^4} \left| \frac{\partial^{m_f}}{\partial \xi^{m_f}} \widehat{f}_Q(\xi) \right|^2 d\xi \\ & \leq C_{m_\gamma} 2^{-m_{\gamma_1} j} 2^{-|m_\gamma|j} (1 + \ell_2)^{m_{\gamma_1}} \int_{\mathbb{R}^4} \left| \frac{\partial^{m_{f_1}}}{\partial \xi_1^{m_{f_1}}} \frac{\partial^{m_{f_2}}}{\partial \xi_2^{m_{f_2}}} \frac{\partial^{m_{f_3}}}{\partial \xi_3^{m_{f_3}}} \widehat{h}_Q(\xi_1, \xi_2, \xi_3) \right|^2 d\xi \\ & = C_{m_\gamma} 2^{-m_{\gamma_1} j} 2^{-|m_\gamma|j} (1 + \ell_2)^{m_{\gamma_1}} \int_{I_{\phi'}} \int_{2^{2j-4}}^{2^{2j+2}} \int_0^{2\pi} r^2 |\sin \theta'| \\ & \quad \times \left| \frac{\partial^{m_{f_1}}}{\partial \xi_1^{m_{f_1}}} \frac{\partial^{m_{f_2}}}{\partial \xi_2^{m_{f_2}}} \frac{\partial^{m_{f_3}}}{\partial \xi_3^{m_{f_3}}} \widehat{h}_Q(r, \theta', \phi') \right|^2 d\theta' dr d\phi' \\ & \leq C_{m_\gamma} 2^{-m_{\gamma_1} j} 2^{-|m_\gamma|j} (1 + \ell_2)^{m_{\gamma_1}} 2^{4j} \\ & \quad \times \int_{I_{\phi'}} \int_{2^{2j-4}}^{2^{2j+2}} \int_0^{2\pi} \left| \frac{\partial^{m_{f_1}}}{\partial \xi_1^{m_{f_1}}} \frac{\partial^{m_{f_2}}}{\partial \xi_2^{m_{f_2}}} \frac{\partial^{m_{f_3}}}{\partial \xi_3^{m_{f_3}}} \widehat{h}_Q(r, \theta', \phi') \right|^2 d\theta' dr d\phi'. \end{aligned}$$

Next, we apply Lemma 4.1. In the no-intersection case we have

$$\sum_{\ell_1 = -|\ell_2|}^{|\ell_2|} \int_{\mathbb{R}^4} \left| \frac{\partial^{m_f}}{\partial \xi^{m_f}} \widehat{f}_Q(\xi) \right|^2 \left| \frac{\partial^{m_\gamma}}{\partial \xi^{m_\gamma}} \Gamma_{j,\ell}(\xi) \right|^2 d\xi$$

$$\begin{aligned}
&\leq C_{m_\gamma} 2^{-m_{\gamma_1} j} 2^{-|m_\gamma| j} (1 + |\ell_2|)^{m_{\gamma_1}} 2^{4j} \int_{I_{\phi'}} 2^{-2j m_{f_1}} 2^{-12j} d\phi' \\
&= C_{m_\gamma} 2^{-m_{\gamma_1} j} 2^{-|m_\gamma| j} (1 + |\ell_2|)^{m_{\gamma_1}} 2^{-2j m_{f_1}} 2^{-9j}.
\end{aligned}$$

In the intersection case, if  $|\sin \phi'| \leq 2^{1-j}$ , we have

$$\begin{aligned}
&\sum_{\ell_1 = -|\ell_2|}^{|\ell_2|} \int_{\widehat{\mathbb{R}}^4} \left| \frac{\partial^{m_f}}{\partial \xi^{m_f}} \widehat{f}_Q(\xi) \right|^2 \left| \frac{\partial^{m_\gamma}}{\partial \xi^{m_\gamma}} \Gamma_{j,\ell}(\xi) \right|^2 d\xi \\
&\leq C_{m_\gamma} 2^{-m_{\gamma_1} j} 2^{-|m_\gamma| j} (1 + |\ell_2|)^{m_{\gamma_1}} 2^{4j} \int_{I_{\phi'}} 2^{-2j m_1} 2^{-7j} d\phi' \\
&= C_{m_\gamma} 2^{-m_{\gamma_1} j} 2^{-|m_\gamma| j} (1 + |\ell_2|)^{m_{\gamma_1}} 2^{-2j m_{f_1}} 2^{-4j}.
\end{aligned}$$

On the other hand, if  $|\sin \phi'| \geq 2^{1-j}$  (in which case  $2^j |\sin \phi'|$  is equivalent to  $|\ell_2|$ ), then we have

$$\begin{aligned}
&\sum_{\ell_1 = -|\ell_2|}^{|\ell_2|} \int_{\widehat{\mathbb{R}}^4} \left| \frac{\partial^{m_f}}{\partial \xi^{m_f}} \widehat{f}_Q(\xi) \right|^2 \left| \frac{\partial^{m_\gamma}}{\partial \xi^{m_\gamma}} \Gamma_{j,\ell}(\xi) \right|^2 d\xi \\
&\leq C_{m_\gamma} 2^{-m_{\gamma_1} j} 2^{-|m_\gamma| j} (1 + |\ell_2|)^{m_{\gamma_1}} 2^{4j} \int_{I_{\phi'}} 2^{-2j m_1} 2^{-12j} |\sin \phi'|^{-5} d\phi' \\
&\leq C_{m_\gamma} 2^{-m_{\gamma_1} j} 2^{-|m_\gamma| j} (1 + |\ell_2|)^{m_{\gamma_1}} 2^{-2j m_{f_1}} 2^{-4j} |\ell_2|^{-5}.
\end{aligned}$$

This proves the theorem.  $\square$

To prove Theorem 3.3 we use a similar idea to [22] but we need to modify some technical steps to take into account the fourth variable. For that, we introduce the following differential operator:

$$L = \left( I - \left( \frac{2^{2j}}{2\pi(1+|\ell_2|)} \right)^2 \frac{\partial^2}{\partial \xi_1^2} \right) \left( I - \left( \frac{2^j}{2\pi} \right)^2 \frac{\partial^2}{\partial \xi_2^2} \right) \left( I - \left( \frac{2^j}{2\pi} \right)^2 \frac{\partial^2}{\partial \xi_3^2} \right) \left( I - \left( \frac{2^{2j}}{2\pi} \right)^2 \frac{\partial^2}{\partial \xi_4^2} \right) \quad (16)$$

Using Theorem 4.3, a direct computation gives the following result.

**Theorem 4.4.** *Let  $f = h_Q g$ , where  $h_Q$  is a surface fragment given by (14), and  $\Gamma_{j,\ell}$  be given by (15). Then, for  $j \geq 0$  and  $|\ell_2| \leq 2^j$ , we have*

$$\sum_{\ell_1 = -|\ell_2|}^{|\ell_2|} \int_{\widehat{\mathbb{R}}^4} \left| L \left( \widehat{f}(\xi) \Gamma_{j,\ell}(\xi) \right) \right|^2 d\xi \leq C 2^{-4j} (1 + |\ell_2|)^{-5}.$$

As observed above, Theorem 4.4 gives an estimate valid for  $f$  in the region  $\mathcal{P}_1$ . A very similar estimate can be derived for the regions  $\mathcal{P}_2$  and  $\mathcal{P}_3$ , using appropriate modifications of the differential operator  $L$ .

#### 4.2. Proof of Theorem 3.3

Fix  $j \geq 0$ . By our remark above, it is enough to consider the region  $\mathcal{P}_1$  only. For  $\mu \in M_j$ , the shearlet coefficients of  $f_Q$  associated to  $\mathcal{P}_1$  can be written as

$$\langle f_Q, \tilde{\psi}_\mu \rangle = \langle f_Q, \psi_{j,k,\ell}^{(1)} \rangle = |\det A_{(1)}|^{-j/2} \int_{\widehat{\mathbb{R}}^4} \widehat{f}(\xi) \Gamma_{j,\ell}(\xi) e^{2\pi i \xi A_{(1)}^{-j} B_{(1)}^{[-\ell]} k} d\xi$$

where  $\Gamma_{j,\ell}$  is given by (15). Using the equivalent definition of the weak  $\ell^1$  norm, we need to show

$$\#\{\mu \in M_j : |\langle f, \tilde{\psi}_\mu \rangle| > \epsilon\} \leq C 2^{-2j} \epsilon^{-1}. \quad (17)$$

We observe that  $\xi A_{(1)}^{-j} B_{(1)}^{-[\ell]} k = (k_1 - k_2 \ell_1 - k_3 \ell_2) 2^{-2j} \xi_1 + k_2 2^{-j} \xi_2 + k_3 2^{-j} \xi_3 + k_4 2^{-2j} \xi_4$ . Hence, letting  $L$  to be the differential operator in (16) and denoting  $E_1(\xi) = e^{2\pi i \xi A_{(1)}^{-j} B_{(1)}^{-[\ell]} k}$  we have that

$$L(E_1(\xi)) = \left(1 + \left(\frac{|\ell_2|}{1+|\ell_2|}\right)^2 \left(\frac{k_1}{|\ell_2|} - \frac{k_2 \ell_1}{|\ell_2|} \pm k_3\right)^2\right) (1 + k_1^2)(1 + k_3)^2(1 + k_4)^2 E_1(\xi)$$

if  $\ell_2 \neq 0$ . Otherwise, if  $\ell_2 = 0$ , we have

$$L(E_1(\xi)) = (1 + k_1^2)(1 + k_1^2)(1 + k_3)^2(1 + k_4)^2 E_1(\xi).$$

Also, a direct computation shows that

$$\langle f, \tilde{\psi}_\mu \rangle = |\det(A_{(1)})|^{-j/2} \int_{\widehat{\mathbb{R}}^4} L(\widehat{f}(\xi) \Gamma_{j,\ell}(\xi)) L^{-1}\left(e^{2\pi i \xi A_{(1)}^{-j} B_{(1)}^{-[\ell]} k}\right) d\xi.$$

We next consider the case where  $\ell_2 \neq 0$ . In this case, we have

$$L^{-1}\left(e^{2\pi i \xi A_{(1)}^{-j} B_{(1)}^{-[\ell]} k}\right) = G(k, \ell)^{-1} e^{2\pi i \xi A_{(1)}^{-j} B_{(1)}^{-[\ell]} k},$$

where  $G(k, \ell) = \left(1 + \left(\frac{|\ell_2|}{1+|\ell_2|}\right)^2 \left(\frac{k_1}{|\ell_2|} - \frac{k_2 \ell_1}{|\ell_2|} \pm k_3\right)^2\right) (1 + k_1^2)(1 + k_3^2)(1 + k_4^2)$ .

Therefore,

$$G(k, \ell) \langle f, \tilde{\psi}_\mu \rangle = |\det(A_{(1)})|^{-j/2} \int_{\widehat{\mathbb{R}}^4} L(\widehat{f}(\xi) \Gamma_{j,\ell}(\xi)) e^{2\pi i \xi A_{(1)}^{-j} B_{(1)}^{-[\ell]} k} d\xi.$$

Let  $K = (K_1, K_2, K_3, K_4) \in \mathbb{Z}^4$  and define

$$\begin{aligned} R_K &= \{k = (k_1, k_2, k_3, k_4) \in \mathbb{Z}^4 : \frac{k_1}{|\ell_2|} \in [K_1, K_1 + 1], -\frac{k_2 \ell_1}{|\ell_2|} \in [K_2, K_2 + 1], \\ &\quad k_3 = K_3, k_4 = K_4\}. \end{aligned}$$

For fixed  $j, \ell$ , the set  $\{|\det A_{(1)}|^{-j/2} e^{2\pi i \xi A_{(1)}^{-j} B_{(1)}^{-[\ell]} k} : k \in \mathbb{Z}^4\}$  is an orthonormal basis for  $L^2$  functions defined on  $[-1/2, 1/2]^4 B_{(1)}^{[\ell]} A_{(1)}^j$  (which contains the support of  $\Gamma_{j,\ell}$ ). It follows that

$$\begin{aligned} \sum_{k \in R_K} G(k, \ell)^2 |\langle f, \tilde{\psi} \rangle|^2 &= \sum_{k \in R_K} |\det(A_{(1)})|^{-j} \left| \int_{\widehat{\mathbb{R}}^4} L(\widehat{f}(\xi) \Gamma_{j,\ell}(\xi)) e^{2\pi i \xi A_{(1)}^{-j} B_{(1)}^{-[\ell]} k} d\xi \right|^2 \\ &\leq \|L(\widehat{f} \Gamma_{j,\ell})\|^2 \\ &= \int_{\widehat{\mathbb{R}}^4} \left| L(\widehat{f}(\xi) \Gamma_{j,\ell}(\xi)) \right|^2 d\xi. \end{aligned}$$

Therefore,

$$\begin{aligned}
& \sum_{\ell_1=-|\ell_2|}^{|\ell_2|} \sum_{k \in R_K} |\langle f, \tilde{\psi} \rangle|^2 \\
&= \sum_{\ell_1=-|\ell_2|}^{|\ell_2|} \sum_{k \in R_K} G(k, \ell)^{-2} |\det(A_{(1)})^{-j}| \left| \int_{\widehat{\mathbb{R}}^4} L(\widehat{f}(\xi) \Gamma_{j, \ell}(\xi)) e^{2\pi i \xi A_{(1)}^{-j} B_{(1)}^{-[\ell]} k} d\xi \right|^2 \\
&\leq C (1 + (K_1 + K_2 \pm K_3)^2)^{-2} (1 + K_2^2)^{-2} (1 + K_3^2)^{-2} (1 + K_4^2)^{-2} \\
&\times \sum_{\ell_1=-|\ell_2|}^{|\ell_2|} \int_{\widehat{\mathbb{R}}^4} |L(\widehat{f}(\xi) \Gamma_{j, \ell}(\xi))|^2 d\xi.
\end{aligned}$$

Using Theorem 4.4, we have

$$\sum_{\ell_1=-|\ell_2|}^{|\ell_2|} \sum_{k \in R_K} |\langle f, \tilde{\psi} \rangle|^2 \leq L_K^{-2} C 2^{-4j} (1 + |\ell_2|)^{-5},$$

where  $L_K = (1 + (K_1 + K_2 \pm K_3)^2) (1 + K_2^2) (1 + K_3^2) (1 + K_4^2)$ . For fixed  $j$  and  $\ell$ , we let  $R_{K, \epsilon} = \{k \in R_K : |\langle f, \psi_{j, k, \ell}^{(1)} \rangle| > \epsilon\}$  and  $N_{j, \ell, K}(\epsilon) = \#R_{K, \epsilon}$ . Then, by the condition  $|\ell_1| \leq |\ell_2|$ , we have that  $N_{j, k, \ell}(\epsilon) \leq C(1 + |\ell_2|)^2$  and, thus,  $\sum_{\ell_1=-|\ell_2|}^{|\ell_2|} N_{j, k, \ell}(\epsilon) \leq (1 + |\ell_2|)^3$ . Now, for  $k \in R_K$  such that  $|\langle f, \psi_{j, k, \ell}^{(1)} \rangle| > \epsilon$ , we have

$$\epsilon^2 N_{j, \ell, K}(\epsilon) \leq \sum_{k \in R_{K, \epsilon}} |\langle f, \tilde{\psi} \rangle|^2 \leq \sum_{k \in R_K} |\langle f, \tilde{\psi} \rangle|^2,$$

which implies

$$\sum_{\ell_1=-|\ell_2|}^{|\ell_2|} N_{j, \ell, K}(\epsilon) \leq L_K^{-2} C 2^{-4j} (1 + |\ell_2|)^{-5} \epsilon^{-2}.$$

Hence

$$\sum_{\ell_1=-|\ell_2|}^{|\ell_2|} N_{j, \ell, K}(\epsilon) \leq C \min((1 + |\ell_2|)^3, L_K^{-2} 2^{-4j} (1 + |\ell_2|)^{-5} \epsilon^{-2}).$$

Now, let  $\ell_2^*$  be defined by  $(\ell_2^* + 1)^3 = L_K^{-2} 2^{-4j} \epsilon^{-2} (1 + \ell_2^*)^{-5}$ , so  $(1 + \ell_2^*)^4 = L_K^{-1} 2^{-2j} \epsilon^{-1}$ . Then,

$$\begin{aligned}
& \sum_{\ell_2=-2^j}^{2^j} \sum_{\ell_1=-|\ell_2|}^{|\ell_2|} N_{j, \ell, K}(\epsilon) \\
&\leq \sum_{|\ell_2| \leq (\ell_2^* + 1)} \sum_{\ell_1=-|\ell_2|}^{|\ell_2|} N_{j, \ell, K}(\epsilon) + \sum_{|\ell_2| > (\ell_2^* + 1)} \sum_{\ell_1=-|\ell_2|}^{|\ell_2|} N_{j, \ell, K}(\epsilon)
\end{aligned}$$

$$\begin{aligned}
&\leq C \sum_{|\ell_2| \leq (\ell_2^* + 1)} (|\ell_2| + 1)^3 + C \sum_{|\ell_2| > (\ell_2^* + 1)} L_K^{-2} 2^{-4j} \epsilon^{-2} (1 + |\ell_2|)^{-5} \\
&\leq C (\ell_2^* + 1)^4 + C L_K^{-2} 2^{-4j} \epsilon^{-2} (1 + \ell_2^*)^{-4} \\
&\leq C L_K^{-1} 2^{-2j} \epsilon^{-1}.
\end{aligned}$$

Notice also that  $\sum_{K \in \mathbb{Z}^4} L_K^{-1} < \infty$ . Thus

$$\begin{aligned}
\#\{\mu \in M_j : |\langle f, \tilde{\psi}_\mu \rangle| > \epsilon\} &\leq \sum_{K \in \mathbb{Z}^4} \sum_{\ell_2 = -2^j}^{2^j} \sum_{\ell_1 = -|\ell_2|}^{|\ell_2|} N_{j, \ell, K}(\epsilon) \\
&\leq C 2^{-2j} \epsilon^{-1} \sum_{K \in \mathbb{Z}^4} L_K^{-1} \leq C 2^{-2j} \epsilon^{-1}
\end{aligned}$$

which gives (17).

Next we consider the case  $\ell_2 = 0$ . In this case, we have

$$L^{-1} \left( e^{2\pi i \xi A_{(1)}^{-j} k} \right) = (1 + k_1^2)(1 + k_2^2)(1 + k_3^2)(1 + k_4^2) e^{2\pi i \xi A_{(1)}^{-j} k}.$$

We let  $L_k = (1 + k_1^2)(1 + k_2^2)(1 + k_3^2)(1 + k_4^2)$  and observe that  $\sum_{k \in \mathbb{Z}^4} L_k^{-1} < \infty$ . A direct computation shows that

$$\langle f, \psi_{j,0,k}^{(1)} \rangle L_k = |\det A_{(1)}|^{-j/2} \int_{\mathbb{R}^4} L \left( \hat{f}(\xi) \Gamma_{j,0}(\xi) \right) e^{2\pi i \xi A_{(1)}^{-j} k} d\xi.$$

From here, using Theorem 4.4, we have that

$$\sum_{k \in \mathbb{Z}^4} L_k^2 |\langle f, \psi_{j,0,k}^{(1)} \rangle|^2 = \int_{\mathbb{R}^4} \left| L \left( \hat{f}(\xi) \Gamma_{j,0}(\xi) \right) \right|^2 d\xi \leq C 2^{-4j}.$$

In particular, for each  $k \in \mathbb{Z}^4$  we have  $|\langle f, \psi_{j,0,k}^{(1)} \rangle| \leq C L_K^{-1} 2^{-2j}$ , and so

$$\| \langle f, \psi_{j,0,k}^{(1)} \rangle \|_1 = \sum_{k \in \mathbb{Z}^4} |\langle f, \psi_{j,0,k}^{(1)} \rangle| \leq C 2^{-2j}$$

which implies  $\| \langle f, \psi_{j,0,k}^{(1)} \rangle \|_{w\ell^1} \leq C 2^{-2j}$ . This concludes the proof of the theorem when  $j \leq j_0$ .

#### 4.3. Analysis of the coarse scale.

At the beginning Section 4, we assumed  $j > j_0$  for some  $j_0 > 0$ . Here we consider the *coarse scale* case  $j \leq j_0$ .

We recall that  $f_Q(x) = h_Q(x_1, x_2, x_3) g(x_4)$  where

$$h_Q(x_1, x_2, x_3) = w(2^j x) h(x_1, x_2, x_3) \mathcal{X}_{\{x_1 > E(x_2, x_3)\}}(x_1, x_2, x_3)$$

with  $w \in C^\infty([-1, 1]^3)$ ,  $h \in C^2([0, 1]^3)$ ,  $g \in C^2([0, 1])$ . Therefore, observing that  $\text{supp } h_Q \in [-2^{-j}, 2^{-j}]^3$  and  $g$  is also compactly supported, we have

$$\|f_Q\|_2^2 \leq \int_{\text{supp}(h_Q) \times \text{supp}(g)} |f_Q(x)|^2 dx \leq C 2^{-3j}.$$

The last inequality implies that  $\|\langle f_Q, \tilde{\psi}_\mu \rangle\|_{\ell^2} \leq \|f_Q\|_2 \leq C 2^{-3j/2}$ . We also notice that

$$\|\langle f_Q, \tilde{\psi}_\mu \rangle\|_{\ell^p} \leq N^{1/p-1/2} \|\langle f_Q, \tilde{\psi}_\mu \rangle\|_{\ell^2}$$

is valid for any sequence  $\{\langle f_Q, \tilde{\psi}_\mu \rangle\}$  of  $N$  elements. Since, at scale  $2^{-j}$ , there are about  $2^{2j}$  shearlet elements in  $Q_j^0$ , so we conclude that there is a constant  $C$  independent of  $Q$  and  $j$  such that

$$\|\langle f_Q, \tilde{\psi}_\mu \rangle\|_{\ell^1} \leq C 2^{2j(1-1/2)} 2^{-3/2j} = C 2^{-j/2}.$$

This completes the proof of Theorem 3.3 for  $j > j_0$ .

#### 4.4. Proof of Theorem 3.4.

We again write  $h_Q(x_1, x_2, x_3) = h(x_1, x_2, x_3)w_Q(x_1, x_2, x_3)$  where we now assume  $Q \in \mathcal{Q}_j^1$ . With this notation, we write the localized function  $f_Q$  as  $f_Q(x_1, x_2, x_3, x_4) = h_Q(x_1, x_2, x_3)g(x_4)$ . The following two lemmata can be proved using an argument very similar to Lemma 4.8 and Lemma 4.9 in [22].

**Lemma 4.5.** *Let  $f_Q = fw_Q$  where  $f = h\mathcal{X}_{Bg} \in \mathcal{E}(A)$  is given by (10),  $Q \in \mathcal{Q}_j^1$  and  $U_{j,\ell}$  be given by (5). Then,*

$$\int_{U_{j,\ell}} |\hat{f}_Q(\xi)|^2 d\xi \leq C 2^{-11j}.$$

**Lemma 4.6.** *Let  $m = (m_1, m_2, m_3, m_4) \in \mathbb{N}^4$ ,  $\xi = (\xi_1, \xi_2, \xi_3, \xi_4) \in \mathbb{R}^4$  and  $\Gamma_{j,\ell}$  given by (15) where  $\ell = (\ell_1, \ell_2)$ . Then,*

$$\sum_{\ell_1=2^j}^{2^j} \sum_{\ell_2=-2^j}^{2^j} \left| \frac{\partial^m}{\partial \xi^m} \Gamma_{j,\ell}(\xi) \right|^2 \leq C_m 2^{-|m|j},$$

where  $C_m$  is independent of  $j$  and  $\xi$ , and  $|m| = m_1 + m_2 + m_3 + m_4$ .

By Lemmata 4.5 and 4.6, using an argument similar to the proof of Lemma 4.10 in [22], we have the following result.

**Lemma 4.7.** *Let  $f_Q = fw_Q$  where  $f \in \mathcal{E}^2(A)$  and  $Q \in \mathcal{Q}_j^1$  and set*

$$T = \left( I - \frac{2^{2j}}{(2\pi)^2} \Delta \right) \tag{18}$$

where  $\Delta = \frac{\partial^2}{\partial \xi_1^2} + \frac{\partial^2}{\partial \xi_2^2} + \frac{\partial^2}{\partial \xi_3^2} + \frac{\partial^2}{\partial \xi_4^2}$ . Then,

$$\int_{\mathbb{R}^4} \sum_{\ell_1=2^j}^{2^j} \sum_{\ell_2=-2^j}^{2^j} \left| T^2 \left( \hat{f}_Q \Gamma_{j,\ell} \right) (\xi) \right|^2 d\xi \leq C 2^{-11j}.$$

Now we prove Theorem 3.4 by adapting the general ideas from [22].

**Proof of Theorem 3.4.**

As observed above, it will be sufficient to consider the system of interior shearlets in the pyramidal region  $\mathcal{P}_1$  as the other pyramidal regions and the boundary shearlets can be handled in a similar way.

For  $T$  given by (18), denoting  $E_1(\xi) = e^{2\pi i \xi A_{(1)}^{-j} B_{(1)}^{-[\ell]} k}$ , we have

$$\begin{aligned} T(E_1(\xi)) &= (1 + 2^{-2j}(k_1 - \ell_1 k_2 - \ell_2 k_3)^2 + k_2^2 + k_3^2 + 2^{-2j} k_4^2) E_1(\xi) \\ T^2(E_1(\xi)) &= (1 + 2^{-2j}(k_1 - \ell_1 k_2 - \ell_2 k_3)^2 + k_2^2 + k_3^2 + 2^{-2j} k_4^2)^2 E_1(\xi). \end{aligned}$$

For a fixed  $j \geq 0$  and  $f_Q = f w_Q$  where  $f = hg$  and  $Q \in \mathcal{Q}_j^1$ , using integration by parts we have

$$\begin{aligned} \langle f_Q, \tilde{\psi}_\mu \rangle &= |\det A_{(1)}|^{-j/2} \int_{\widehat{\mathbb{R}}^4} \widehat{f}_Q(\xi) \Gamma_{j,\ell}(\xi) e^{2\pi i \xi A_{(1)}^{-j} B_{(1)}^{-[\ell]} k} d\xi \\ &= |\det A_{(1)}|^{-j/2} (1 + 2^{-2j}(k_1 - \ell_1 k_2 - \ell_2 k_3)^2 + k_2^2 + k_3^2 + 2^{-2j} k_4^2)^{-2} \\ &\quad \times \int_{\widehat{\mathbb{R}}^4} T^2(\widehat{f}_Q(\xi) \Gamma_{j,\ell}(\xi)) e^{2\pi i \xi A_{(1)}^{-j} B_{(1)}^{-[\ell]} k} d\xi. \end{aligned}$$

Now, for  $K = (K_1, K_2, K_3, K_4) \in \mathbb{Z}^4$  we set

$$\begin{aligned} R_K &= \{(k_1, k_2, k_3, k_4) \in \mathbb{Z}^4 : k_3 = K_3, k_2 = K_2, \\ &\quad 2^{-j} k_4 \in [K_4, K_4 + 1], 2^{-j}(k_1 - K_2 \ell_1 - K_3 \ell_2) \in [K_1, K_1 + 1]\}. \end{aligned}$$

We observe that  $2^j K_1 \leq k_1 - K_2 \ell_1 - K_3 \ell_2 \leq 2^j(K_1 + 1)$  and  $2^j K_4 \leq k_4 \leq 2^j(K_4 + 1)$ , so for each  $K$  and  $\ell$  there are only  $1 + 2^j$  choices for  $k_1$  and  $k_4$  in  $R_K$ . Thus, the number of elements of  $R_K$  is bounded by  $(2^j + 1)^2$ . We next use an argument similar to the proof of Theorem 3.3 above. We observe that, for fixed  $j$  and  $\ell$  the set  $\{|\det A_{(1)}|^{-j/2} e^{2\pi i \xi A_{(1)}^{-j} B_{(1)}^{-[\ell]} k} : k \in \mathbb{Z}^4\}$  is an orthonormal basis for the  $L^2$  functions supported on  $[-1/2, 1/2] B_{(1)}^{[\ell]} A_{(1)}^j$ . Furthermore, we note that  $\Gamma_{j,\ell}$  is supported on  $[-1/2, 1/2] B_{(1)}^{[\ell]} A_{(1)}^j$ . Thus

$$\begin{aligned} \sum_{k \in R_K} |\langle f_Q, \tilde{\psi}_\mu \rangle|^2 &= 2^{-6j} \sum_{k \in R_K} (1 + 2^{-2j}(k_1 - \ell_1 k_2 - \ell_2 k_3)^2 + k_2^2 + k_3^2 + 2^{-2j} k_4^2)^{-2} \\ &\quad \times \left| \int_{\widehat{\mathbb{R}}^4} T^2(\widehat{f}_Q(\xi) \Gamma_{j,\ell}(\xi)) e^{2\pi i \xi A_{(1)}^{-j} B_{(1)}^{-[\ell]} k} d\xi \right|^2 \\ &\leq 2^{-6j} (1 + K_1^2 + K_2^2 + K_3^2 + K_4^2)^{-4} \int_{\widehat{\mathbb{R}}^4} \left| T^2(\widehat{f}_Q(\xi) \Gamma_{j,\ell}(\xi)) \right|^2 d\xi. \end{aligned}$$

From the last inequality, using lemma 4.7 we see that

$$\sum_{\ell_2 = -2^j}^{2^j} \sum_{\ell_1 = -2^j}^{2^j} \sum_{k \in R_K} |\langle f_Q, \tilde{\psi}_\mu \rangle|^2 \leq C(1 + K_1^2 + K_2^2 + K_3^2 + K_4^2)^{-4}$$

$$\begin{aligned}
& \times \int_{\widehat{\mathbb{R}}^4} \sum_{\ell_2=-2^j}^{2^j} \sum_{\ell_1=-2^j}^{2^j} \left| T^2 \left( \widehat{f}_Q(\xi) \Gamma_{j,\ell}(\xi) \right) \right|^2 d\xi \\
& \leq C(1 + K_1^2 + K_2^2 + K_3^2 + K_4^2)^{-4} 2^{-11j}. \quad (19)
\end{aligned}$$

By the Hölder inequality, we have that for any  $N \in \mathbb{N}$

$$\sum_{m=1}^N |a_m| \leq \left( \sum_{m=1}^N |a_m|^2 \right)^{1/2} N^{1/2}.$$

Thus, using the last inequality with (19) and the observation that the number of elements of  $R_K$  is bounded by  $(1 + 2^j)^2$ , we have

$$\begin{aligned}
\sum_{\ell_2=-2^j}^{2^j} \sum_{\ell_1=-2^j}^{2^j} \sum_{k \in R_K} |\langle f_Q, \tilde{\psi}_\mu \rangle| & \leq (2^{4j})^{1/2} \left( \sum_{\ell_2=-2^j}^{2^j} \sum_{\ell_1=-2^j}^{2^j} \sum_{k \in R_K} |\langle f_Q, \tilde{\psi}_\mu \rangle|^2 \right)^{1/2} \\
& \leq 2^{2j} C(1 + K_1^2 + K_2^2 + K_3^2 + K_4^2)^{-2} 2^{-11j/2}.
\end{aligned}$$

This shows that, for  $f_Q = fw_Q$  with  $Q \in \mathcal{Q}_j^1$  we have  $\sum_{\mu \in M_j} |\langle f_Q, \tilde{\psi}_\mu \rangle| \leq C2^{-7j/2}$ . This completes the proof of theorem.  $\square$

## 5. Numerical implementation of 4d cylindrical shearlet

This section covers the practical implementation of the 4d cylindrical shearlet transform, including its inverse and adjoint transform, which we apply in Sec. 6 to illustrate the potentiality of cylindrical shearlets in numerical applications. Here, we give a general overview of the implementation: working codes for the Matlab framework, with all the necessary documentation, are available in Github [25].

Key ideas of the implementation generalize those of the 3d cylindrical shearlet transform [19] and are illustrated by the decomposition scheme in Fig. 1. The directional filters, in particular, are derived from the 3d discrete shearlets [17], since the directional structure only affects the first three dimensions. We point out that the current implementation is meant as a proof of concept and possible solutions to the evident inefficiencies are left for future work.

In the following, we denote discrete values at a specific (multi-)index by using square brackets  $[\cdot]$ . Operations like the inner product  $\langle \cdot, \cdot \rangle$ , the discrete Fourier transform  $\mathcal{F}(x)[\xi] = \widehat{x}[\xi]$  and its inverse  $\mathcal{F}^{-1}(x) = \check{x}$  are defined as usual, unless otherwise specified. Given a discretized 4d object  $\mathbf{f}$  and  $J, \ell, k$  fixed (notice that these indexes depend on the resolution and user inputs), the forward transform  $\mathcal{S}$  can be computed using the following steps:

1. **Subband decomposition.** Compute the 4d multilevel (up to scale  $J$ ) subband decomposition  $\mathcal{P}_J \mathbf{f} = (\mathbf{f}_j)_{j=0}^J$  using an adapted Laplacian pyra-

mid scheme<sup>1</sup>. In the frequency domain, each subband corresponds to a windowing:

$$\widehat{\mathbf{f}}_j[k] = \widehat{\mathbf{f}}[k]\mathbf{W}_j[k].$$

This operation corresponds to the first part of equation (4) in the construction of the Parseval frame Sec. 2.1.

2. **Directional filtering.** Consistently with Definition 2.1 and following the approach in [17], we construct the directional filters  $\mathbf{V}_{j,\ell}^{(d)}$ , for given scale  $j$ , direction  $\ell = (\ell_1, \ell_2)$  and cylindrical hyperpyramid indexed by  $d$ , by first defining a window in the pseudo-spherical Fourier domain and then resampling on the Cartesian grid. Note that the directional filters are (approximately) symmetric and, due to the construction, the decomposed signal does not need to be resampled.
3. **Transform coefficients.** Using the directional filters, the cylindrical shearlet coefficients are thus given by:

$$\mathcal{S}(\mathbf{f}) := \langle \mathbf{f}, \psi_{j,\ell,k}^{(d)} \rangle = \mathbf{f}_j *_{3d} \check{\mathbf{V}}_{j,\ell}^{(d)}[k] = \mathcal{F}^{-1} \left( \widehat{\mathbf{f}}_j[k] \mathbf{V}_{j,\ell}^{(d)}[k] \right), \quad (20)$$

where  $k = (k_1, k_2, k_3, k_4) \in \mathbb{Z}^4$  and  $*_{3d}$  denotes discrete convolution along the first three dimensions.

In step 2, the initial construction of the  $\mathbf{V}_{j,\ell}^{(d)}$ 's does not guarantee that the sizes match the size of  $\widehat{\mathbf{f}}_j$ . Hence, the necessary padding and many FFTs required slow down the algorithm considerably. In our experiments to perform step 3, we found that performing the cylindrical (3d) convolution as a point-wise multiplication in the Fourier domain is still more efficient than a direct convolution in the spatial domain.

From the cylindrical shearlet coefficients (20), the original 4d signal  $\mathbf{f}$  can be recovered using the inverse cylindrical shearlet transform  $\mathcal{S}^{-1}$ . By design of the directional filters, for each scale  $j$  we have:

$$\sum_{d=1}^3 \sum_{\ell} \mathbf{V}_{j,\ell}^{(d)} = 1.$$

Hence, the inverse transform is very straightforward to compute since we have:

$$\sum_{d=1}^3 \sum_{\ell} \langle \mathbf{f}, \psi_{j,\ell,\cdot}^{(d)} \rangle = \sum_{d=1}^3 \sum_{\ell} \mathcal{F}^{-1} \left( \widehat{\mathbf{f}}_j[k] \mathbf{V}_{j,\ell}^{(d)}[k] \right) = \mathbf{f}_j,$$

which in turn yields

$$\mathbf{f} = \mathcal{S}^{-1} \left( \langle \mathbf{f}, \psi_{j,\ell,k}^{(d)} \rangle \right) := \mathcal{P}_J^{-1} \left( \sum_{d=1}^3 \sum_{\ell} \langle \mathbf{f}, \psi_{j,\ell,\cdot}^{(d)} \rangle \right), \quad (21)$$

---

<sup>1</sup>This particular implementation of the Laplacian pyramid decomposition was originally introduced for the surfacelet transform [26] and here we follow [19] in applying the same idea to cylindrical shearlets.

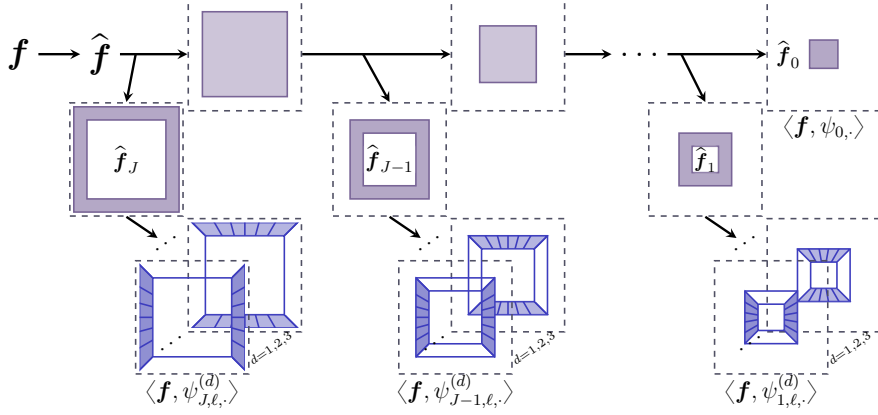


Figure 1: Illustration of how the (cylindrical) shearlet transform decomposes the input signal. The signal is split into  $J + 1$  subbands in the Fourier domain using the Laplacian pyramid scheme (step 1). Next, the cylindrical shearlet coefficients are computed for all scales, orientations and hyperpyramids (step 3) using directional filters associated with the three hyperpyramids and different shearing parameters  $\ell = (\ell_1, \ell_2)$  (created in step 2).

where  $\mathcal{P}_J^{-1}$  is the inverse of the Laplacian pyramid-like scheme. No convolutions or filters are needed making this computation is very efficient.

Finally, we discuss how we implemented the adjoint (or synthesis) operator  $\mathcal{S}^*$  whose computation is somewhat burdensome compared to the inverse. First let  $\mathbf{u}_{j,\ell,d}[k]$  be a vector on the cylindrical shearlet coefficient domain. Then a direct computation of the inner product gives:

$$\begin{aligned}
\langle \mathcal{S}(\mathbf{f}), \mathbf{u}_{j,\ell,d} \rangle &= \sum_{j=0}^J \sum_{d=1}^3 \sum_{\ell} \langle \langle \mathbf{f}, \psi_{j,\ell,\cdot}^{(d)} \rangle, \mathbf{u}_{j,\ell,d} \rangle \\
&= \sum_{j=0}^J \sum_{d=1}^3 \sum_{\ell} \langle \mathbf{f}_j *_{3d} \tilde{\mathbf{V}}_{j,\ell}^{(d)}, \mathbf{u}_{j,\ell,d} \rangle \\
&= \sum_{j=0}^J \langle \mathbf{f}_j, \sum_{d=1}^3 \sum_{\ell} \mathbf{u}_{j,\ell,d} *_{3d} \Lambda_{j,\ell}^{(d)} \rangle \\
&= \langle \mathbf{f}, \mathcal{P}_J^* \left( \sum_{d=1}^3 \sum_{\ell} \mathbf{u}_{j,\ell,d} *_{3d} \Lambda_{j,\ell}^{(d)} \right) \rangle \\
&= \langle \mathbf{f}, \mathcal{S}^{-1} \left( \mathbf{u}_{j,\ell,d} *_{3d} \Lambda_{j,\ell}^{(d)} \right) \rangle,
\end{aligned}$$

where  $\Lambda_{j,\ell}^{(d)}[k_1, k_2, k_3, k_4] := \tilde{\mathbf{V}}_{j,\ell}^{(d)}[-k_1, -k_2, -k_3, k_4] \approx \tilde{\mathbf{V}}_{j,\ell}^{(d)}[k_1, k_2, k_3, k_4]$  by symmetry. The last step follows from equation (21) and the observation that, unlike a traditional Laplacian pyramid decomposition (cf. [27]), the implementation in [26] has the property that  $\mathcal{P}_J^* = \mathcal{P}_J^{-1}$ ; this simplifies the final implementation step. However, computing the adjoint is slower than the inverse and

may produce blurring artifacts due to the convolutions involved.

## 6. An application to dynamic tomography

In this section, we illustrate the numerical advantages of cylindrical shearlets vs. conventional 4d wavelets when dealing with spatio-temporal data whose geometry is consistent with the model of cylindrical cartoon-like functions by considering a challenging inverse problem, namely the reconstruction of a volume over time associated with 4d (3d+time) dynamic CT.

CT is a classical inverse problem concerned with recovering the inner structure of an unknown object from external measurements of its X-ray attenuation intensity. This task is notoriously ill-posed, especially when measurements are sparse. One way to overcome ill-posedness and, thus, to guarantee a stable and unique solution, is to add *regularization* to the problem [28]. During the last decade, several sparse regularization strategies were proposed in CT applications, based on the paradigm that, for each class of data, there exists an appropriate sparsifying representation such as wavelets or shearlets.

Here we illustrate the application of a regularizer based on cylindrical shearlets to dynamic CT by adapting to the 3d+time setting a regularized reconstruction method based on (conventional) shearlets proposed by some of the authors in [16]. This reconstruction method was originally motivated by sparse imaging of phloem transport in plant stems and was shown to be extremely competitive as compared to other methods from the literature. One advantage of this approach is that it is not limited to 2d data, like many existing methods [29, 30], and does not require dense angular sampling as the approaches relying on filtered back-projection (FBP), cf. [31, 32, 33, 34]. Additionally, we do not need to assume periodicity on the movement as in [35], nor constant total brightness as compared to optical flow [36] nor multiple source-detector pairs, as in [37, 38].

We refer the interested reader to [39] for a broader overview of image reconstruction in dynamic inverse problems.

### 6.1. Mathematical model

Modern cone-beam CT scanners collect 2d projection images from given angle views. These projections can then be used to reconstruct a 3d volume of the interior attenuation of the targeted object. If this measurement process is then repeated over time, the object of interest can be understood as a 4d object. As observed above, given the sparse measurements and the violation of the static assumption that it is often assumed in classical CT reconstruction schemes, stable recovery of a moving object from multiple sparse measurements over a given time period requires regularization.

By applying 4d cylindrical shearlets as regularizer, we do not only regularize over the 3d spatial volume but also across time frames within the same representation system. This is expected to be an advantage with respect to separable representations, as suggested by their superior approximation properties since a lower number of samples is required to achieve the same approximation.

Formally, for each time step  $t = 1, \dots, \tau$ , let  $\mathbf{f}_t[x_1, x_2, x_3] \in \mathbb{R}_+^n$ , with  $n = n_{x_1}n_{x_2}n_{x_3}$ , be a vector representing the unknown 3d object,  $\mathcal{R}_t \in \mathbb{R}^{p \times n}$  a matrix modelling the tomographic cone-beam measurement process and  $\mathbf{m}_t + \boldsymbol{\eta} =: \mathbf{m}_t^\eta \in \mathbb{R}^p$  the data corrupted by measurement errors  $\boldsymbol{\eta} = \boldsymbol{\eta}(t)$ . To further simplify our notation we set:

$$\mathbf{f} = \begin{bmatrix} \mathbf{f}_1 \\ \vdots \\ \mathbf{f}_\tau \end{bmatrix}, \quad \mathcal{R} = \begin{bmatrix} \mathcal{R}_1 & & \\ & \ddots & \\ & & \mathcal{R}_\tau \end{bmatrix}, \quad \mathbf{m}^\eta = \begin{bmatrix} \mathbf{m}_1^\eta \\ \vdots \\ \mathbf{m}_\tau^\eta \end{bmatrix}.$$

Then a regularized solution  $\mathbf{f} \in \mathbb{R}_+^{n\tau}$  can be obtained by minimizing the functional

$$J(\mathbf{f}) = \frac{1}{2} \|\mathcal{R}\mathbf{f} - \mathbf{m}^\eta\|_2^2 + \beta \|\mathcal{S}\mathbf{f}\|_1. \quad (22)$$

Here, the regularization parameter  $\beta > 0$  balances between the data mismatch term over the time steps and the  $\ell^1$ -sparsity of 4d cylindrical shearlet coefficients of the solution.

A robust minimization method is the Primal-Dual Fixed Point (PDFP) algorithm [40], which generalizes the well-known Iterative Soft-Tresholding Algorithm (ISTA) to include non-negativity constraints for the solution  $\mathbf{f}$  and ensures convergence even when the sparsifying system does not form an orthonormal basis but a frame, as it is the case with cylindrical shearlets. By using PDFP, equation (22) can be minimized by iterating the following steps:

$$\begin{aligned} \mathbf{y}^{(i+1)} &= \text{proj}_+(\mathbf{f}^{(i)} - \rho(\mathcal{R}^T \mathcal{R} \mathbf{f}^{(i)} - \mathcal{R}^T \mathbf{m}^\eta) - \lambda \mathcal{S}^* \mathbf{r}^{(i)}), \\ \mathbf{r}^{(i+1)} &= (\mathbb{I} - S_{\beta \frac{\rho}{\lambda}})(\mathcal{S} \mathbf{y}^{(i+1)} + \mathbf{r}^{(i)}), \\ \mathbf{f}^{(i+1)} &= \text{proj}_+(\mathbf{f}^{(i)} - \rho(\mathcal{R}^T \mathcal{R} \mathbf{f}^{(i)} - \mathcal{R}^T \mathbf{m}^\eta) - \lambda \mathcal{S}^* \mathbf{r}^{(i+1)}) \end{aligned} \quad (23)$$

where  $S_{\beta \frac{\rho}{\lambda}}$  denotes the soft-thresholding operator and  $\text{proj}_+$  is the projection onto the non-negative orthant. The parameters  $\rho$  and  $\lambda$  are bounded by properties of the functional  $J$ , which set a clear range for their values, while the optimal choice of  $\beta$  is a notoriously difficult task. Here, we utilize an automated tuning of  $\beta$  based on the a priori given desired sparsity level of the cylindrical shearlet coefficients. This method was first introduced in [41] using Haar wavelet regularization in traditional 2d tomography regularization and contains a detailed explanation of the automated sparsity control. Recently we applied the method to 2d+time dynamic tomography setting using classical shearlets [16] and 3d+time (complex) wavelets [42], where we also motivated the choice of this model further. The detailed steps are summarized in Algorithm 1 in [16], where the necessary modification from 3d to 4d apply.

## 6.2. Simulated test data

Our regularized reconstruction algorithm was applied to a simulated 4d tomography dataset consisting of repeated measurements of a 3d Shepp-Logan phantom [43] which is deformed over time by squishing and stretching the

volume. We remark that this phantom is well approximated by a cylindrical cartoon-like function as the data is dominated by discontinuities in the spatial coordinates.

The spatial dimensions of the volume are  $128 \times 128 \times 128$  voxels and we simulated in total 16 sparse angle cone-beam sinograms. We test varying number of evenly spaced projection angles: in Sec. 6.3, we report results with 24, 30, 45 and 90 equispaced angles. The matrices  $\mathcal{R}_t$  (and therefore  $\mathcal{R}$ ) simulating the geometry of a cone-beam CT are generated using the HelTomo Toolbox [44], build upon the ASTRA Toolbox [45]. The periodic motion depends on a parameter  $\omega \in [0, 2\pi]$  and is inspired by [31]. Given the initial state of the phantom  $\mathbf{f}_0(x_1, x_2, x_3) \in \mathbb{R}_+^n$ , any subsequent state is given by

$$\mathbf{f}_\omega(x_1, x_2, x_3) = \mathbf{f}_0 \left( \frac{x_1}{c_1}, c_1 x_2 + 0.44(1 - c_1), \frac{x_3}{c_2} \right),$$

where

$$c_1 = 0.05 \cdot \cos(\omega) + 0.95 \quad \text{and} \quad c_2 = 0.02 \cdot \cos(\omega) + 0.98.$$

To better approximate continuous motion and realistic measurement conditions we pick samples of  $\omega$  in the following manner. First, given the number of desired measurements (here  $\tau = 16$ ) we divide the whole period of  $[0, 2\pi]$  into  $2\tau - 1$  subintervals and discard every second one leaving a total of  $\tau$  disjoint subintervals. Then, for each  $t$  we further sample the corresponding subinterval to obtain 15 values of  $\omega(t) = (\omega_1^{(t)}, \dots, \omega_{15}^{(t)})$  which are used to simulate the sinogram  $\mathbf{m}_t$  in 15 stages. The middle value from each subinterval (i.e.  $\omega_8^{(t)}$  for each  $t$ ) is taken as the ground truth  $\mathbf{f}_t$  for benchmarking the reconstructions. The sampling procedure is illustrated in Fig. 2.

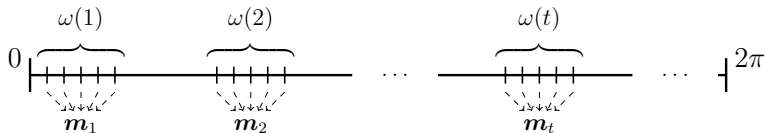


Figure 2: Illustration how multiple values of  $\omega$  are used to simulate measurements at each time frame  $t$ .

The jump in values of  $\omega$  between measurements simulates a pause between consecutive measurement cycles and allows for more noticeable changes between time frames. We illustrate this in Fig. 3 which contains few central horizontal ( $xy$ -plane) slices of the phantom at different time frames  $t$ . In comparison, the changes allowed within each  $t$  are less severe but not negligible as in practice the measurement device can not measure all projections simultaneously.

Finally, to avoid inverse crime, each individual projection image is generated at twice the desired resolution, down-sampled and then corrupted by white Gaussian noise (0 mean and 5% variance).

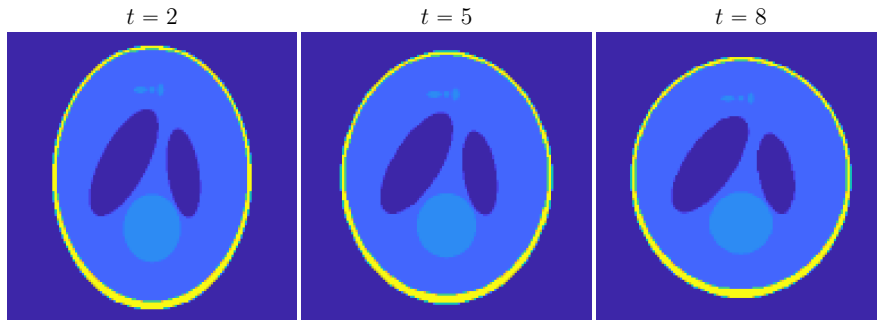


Figure 3: Interior ( $xy$ -plane) slices of the phantom as it evolves over time steps  $t = 2, 5, 8$ .

### 6.3. Results

We report here the numerical results of our reconstruction algorithm for dynamic CT. Results comprise reconstructions from a varied number of sparse projection angles. For comparison purpose, we implemented also a regularized reconstruction algorithm based on the 4d discrete wavelet transform (DWT). The regularized model with 4d DWT is obtained by replacing  $\mathcal{S}$  with a DWT in equation (23) and changing the values of  $\lambda$  and  $\beta$  accordingly. The 4d DWT is implemented by extending the 3d DWT from Matlab’s Wavelet Toolbox and it is available on GitHub [46].

Fig. 4 displays our algorithm reconstructions, using 4d cylindrical shearlets and 4d wavelets regularization methods, of an interior slice of our 3d-phantom for selected time frames. The ground truth is also displayed. Note that, in this figure, the number of projections is fixed to 30. Fig. 5 displays an interior slice the algorithm reconstructions using both regularization methods of an interior slice of our 3d-phantom for a varying number of projections. In this figure, the time frame is fixed to  $t = 2$ .

In both figures we only displayed the reconstruction of the central  $xy$ -plane. Additionally, we included as an insert a zoomed-in sub-region containing multiple sharp boundaries to highlight the reconstruction quality at the discontinuities. Reconstruction along other cross-sections of the solid exhibit similar properties.

We report numerical error metrics in Table 1. Specifically, we computed the Peak-Signal-to-Noise-Ratio (PSNR) comparing the whole 4d reconstruction to the known ground truth. In addition, we used the recently introduced Haar-wavelet Perceptual Similarity Index (HPSI) [47], originally proposed for images (i.e., 2d data) and here adapted to handle our data: namely, for each value of  $t$ , we compare the central slice (shown in the figures) to the central slice of the ground truth and report the mean value across all time frames. Finally, we compute the 3d Structural SIMilarity index (SSIM) [48] and the 3d multi-level SSIM [49] (using three scales) which we also average across all time frames. These error metrics are arguably the most faithful among those in Table 1.

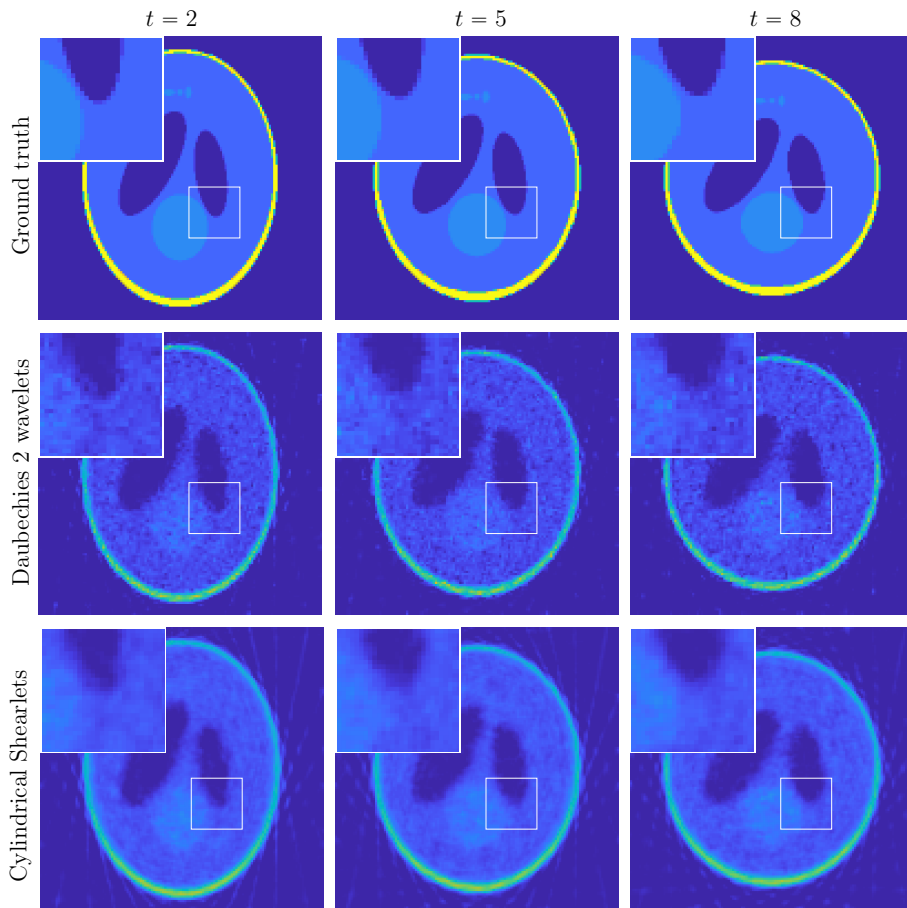


Figure 4: Interior slices of the ground truth (top row), wavelet-regularized solution (center row) and cylindrical shearlet regularized solution (bottom row) evolving over time frames  $t = 2$  (left),  $t = 5$  (middle) and  $t = 8$  (right). All reconstructions from 30 projections.

Results show that overall the cylindrical shearlet regularization yields superior reconstruction both in terms of visual quality and quantitative performance metrics. Visual differences in reconstruction are more pronounced for sparse projections (see Fig. 4, and middle and right columns of Fig. 5) than for denser ones (Fig. 5, left column). Cylindrical shearlets reconstructions are consistently superior at suppressing noise without blurring sharp edges too much while wavelet regularized solutions are noisier. This behavior is especially conspicuous in the bright spherical section in the bottom half of the phantom; this region is hard to discern in the wavelet regularized reconstructions while it is visible in cylindrical shearlets reconstruction. The outer shell of the phantom is relatively well reconstructed with both regularized approaches even though its overall intensity (i.e., brightness) is lower than expected. With sparser projections we also start

to see streaking artifacts outside of the phantom.

Quantitative error measures in Table 1 show that the PSNR favours the cylindrical shearlets, with the exception of 90 projections angles. Cylindrical shearlets also yield better results in all test cases with respect to the (single scale) SSIM and multi-scale SSIM. The mean HPSI estimate, however, is higher for the wavelet regularization, but with sparser angles the difference is very small. We remark that, while none of our error metrics fully accounts for the geometry of 4d spatio-temporal data, the SSIM metrics are the only ones assessing in some form the reconstruction quality of 3d spatial volumes. In fact, SSIM is applied in the literature to measure video approximations (2d + time setting) [50]. On the other hand, PSNR considers only pointwise values with no geometric considerations and HPSI is computed from 2d slices. The topic of image and video quality assessment is a vast and active research area (cf. [51, 52]); it is expected that more adequate and easy-to-use quality metrics for 3d + time data will become available in the future.

Table 2 lists the computation time and number of iterations required to reach the solution. Due to the high memory requirements of the 4d cylindrical shearlet transform, all computations were carried out on the Turso cluster at the University of Helsinki, using 16 CPU cores each equipped with 16GB memory.

Table 1: Numerical error estimates of the different reconstructions.

	Projections	PSNR	Mean HPSI	Mean SSIM	Mean multiSSIM
Daubechies 2-wavelets	90	<b>23.001</b>	<b>0.647</b>	0.889	0.936
	45	21.742	<b>0.596</b>	0.860	0.913
	30	21.110	<b>0.537</b>	0.839	0.898
	24	20.667	<b>0.460</b>	<b>0.806</b>	0.880
Cylindrical shearlets	90	22.432	0.581	<b>0.901</b>	<b>0.941</b>
	45	<b>22.319</b>	0.565	<b>0.876</b>	<b>0.933</b>
	30	<b>22.056</b>	0.521	<b>0.849</b>	<b>0.922</b>
	24	<b>21.411</b>	0.437	<b>0.806</b>	<b>0.894</b>

Table 2: Number of iterations and computational times of the different reconstructions.

	Projections	Iterations	Time:	
			total (min)	per iter. (s)
Daubechies 2-wavelets	90	113	16.1	9
	45	129	24.0	11
	30	140	21.3	9
	24	148	20.7	8
Cylindrical shearlets	90	47	2311.3	2951
	45	50	2459.1	2950
	30	55	2766.6	3018
	24	55	2707.6	2953

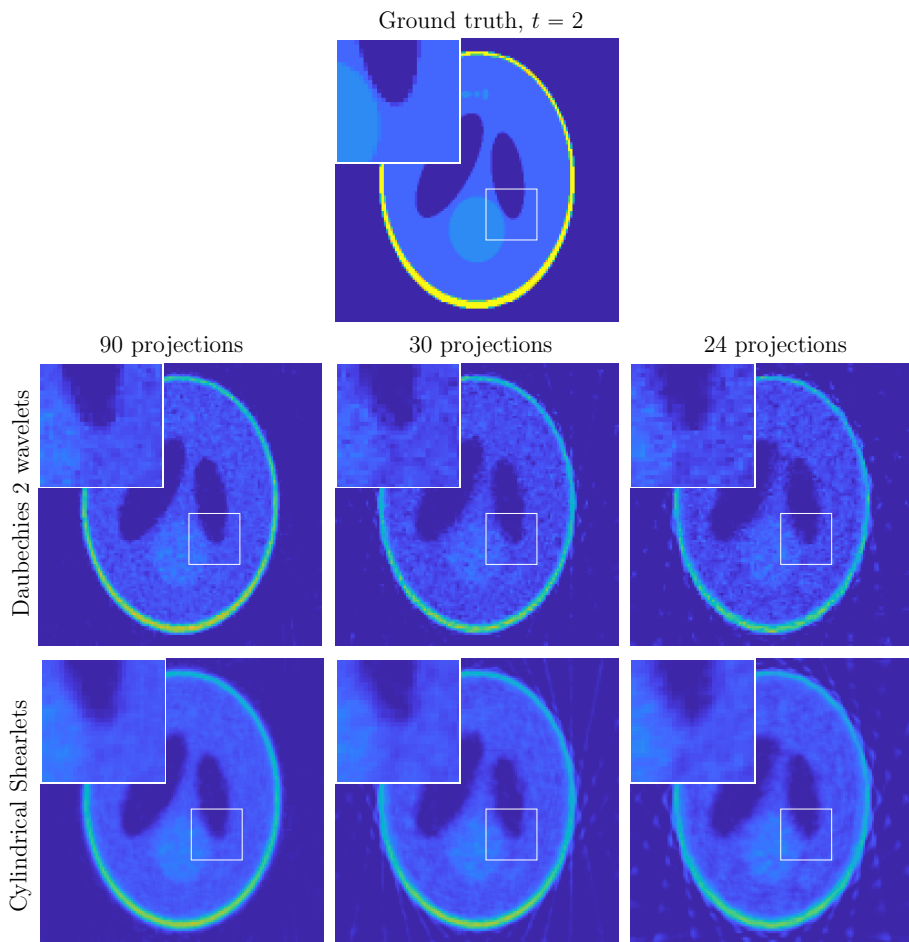


Figure 5: Interior slices at time frame  $t = 2$  of the ground truth (top row), wavelet-regularized solution (center row) and cylindrical shearlet regularized solution (bottom row). On different columns, there are reconstructions from 90 (left), 30 (middle) and 24 (right) projections.

As it is evident from Table 2, the difference in computational burden is considerable. Using the tested data size and current implementation, the computational complexity is infeasible with regular desktop computers. A single computation of the forward, inverse or adjoint transform is doable but iterative schemes usually require applying it tens or hundreds of times, rendering the whole procedure very slow. Finally, also the resolution of the directional filters needs to be sufficiently large to give reliable results. Therefore, low resolution data is not currently a viable alternative to speed up the computations.

## 7. Conclusion

We have introduced a new construction of multiscale representations on  $L^2(\mathbb{R}^4)$  that is especially designed for the efficient approximations of spatio-temporal data and is shown to provide highly sparse representations in the class of 4d-cartoon-like images, significantly outperforming conventional multiscale representations. We have also demonstrated the practical advantages of the new representation on a challenging problem of sparse reconstruction in dynamic tomography using a synthetic phantom. Our numerical results show that our regularized reconstruction based on cylindrical shearlets outperforms a similar algorithm based on wavelets both in terms of visual quality and quantitative performance metric when projections are sparse. We expect that a comparable performance advantage will hold using experimental data and will be investigated in a future work by extending our study of phloem transport in plant stems [16].

As remarked above, the model of cylindrical cartoon-like functions adopted in this paper is a rather crude simplification of temporal sequences of 3-dimensional images, as it does not assume discontinuities with respect to the temporal variable. The phantom we used in our simulations satisfies only approximately this model since discontinuous spatial boundaries evolve smoothly over time. In fact, realistic applications of dynamic CT typically involve boundaries in the spatial domain that change in time so that our model becomes inadequate. We claim, however, that the proofs presented in this work can be extended with a relatively simple argument to include some important generalizations of the cylindrical cartoon-like model such as the situation of a moving solid object, e.g., a moving ball. In this case, the boundary of the object is (smoothly) displaced from a time-frame to the next one, without changes in the discontinuous boundary other than its location being rigidly translated (see Fig. 6 for an illustration in  $\mathbb{R}^3$ ). To model such functions on  $\mathbb{R}^4$ , we may consider a modified cylindrical image model on  $L^2(\mathbb{R}^4)$  where  $f(x_1, x_2, x_3, x_4) = h((x_1, x_2, x_3) - t(x_4))g(x_4)$  where  $h$  is a compactly supported  $C^2$  function away from  $C^2$  boundaries,  $g \in C^2([-1, 1])$  and  $t$  is a smooth translation function which depends on  $x_4$  only. The Fourier transform of  $f$  is of the form  $\hat{f}(\xi_1, \xi_2, \xi_3, \xi_4) = \hat{h}(\xi_1, \xi_2, \xi_3) G(\xi_1, \xi_2, \xi_3, \xi_4)$  where  $G$  is smooth and bounded. From this observation, it follows that one can adapt essentially the same arguments presented above to derive a result very similar to Theorems 3.1 and 3.2. A more detailed discussion of this extension of our proof would require more technical details that are beyond the scope of this paper and, for reasons of space, are left to a future work.

Finally, concerning the topic of numerical reconstruction in dynamic CT, we recall that deep learning strategies have been applied very successfully in inverse problems including CT often in combination with model-based principles such as sparsity models (e.g., [16]). We expect that the ideas presented in this paper are very promising to develop a new generation of reconstruction algorithms for dynamic CT integrating learning- and model-based principles.

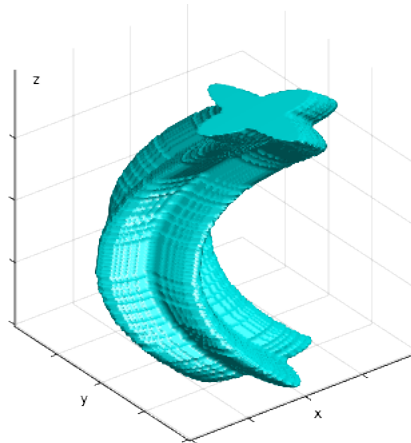


Figure 6: Modified 3-dimensional cartoon-like image. The discontinuous boundary curve in the  $xy$  plane is rigidly displaced as a function of the  $z$  coordinate.

### Acknowledgements

We acknowledge the support of the IT for Science group of the University of Helsinki for the high performance computing cluster Turso. TAB is supported by the Royal Society through the Newton International Fellowship grant n. NIF\R1\201695 and was partially supported by the Academy of Finland through the postdoctoral grant, decision number 330522. DL acknowledges support of NSF-DMS 1720487 and 172045. TH acknowledges support of the Emil Aaltonen Foundation junior researcher grant no. 200029 and the Academy of Finland Project 310822.

### References

- [1] E. J. Candès, D. L. Donoho, New tight frames of curvelets and optimal representations of objects with piecewise  $c^2$  singularities, *Communications on Pure and Applied Mathematics: A Journal Issued by the Courant Institute of Mathematical Sciences* 57 (2) (2004) 219–266.
- [2] K. Guo, D. Labate, Optimally sparse multidimensional representation using shearlets, *SIAM J. Math. Analysis* 39 (2007) 298–318.
- [3] G. Kutyniok, W.-Q. Lim, Compactly supported shearlets are optimally sparse, *Journal of Approximation Theory* 163 (11) (2011) 1564–1589.
- [4] S. Mallat, Geometrical grouplets, *Applied and Computational Harmonic Analysis* 26 (2) (2009) 161–180.
- [5] J. Bruna, S. Mallat, Invariant scattering convolution networks, *IEEE transactions on pattern analysis and machine intelligence* 35 (8) (2013) 1872–1886.

- [6] C. Lessig, P. Petersen, M. Schäfer, Bendlets: A second-order shearlet transform with bent elements, *Applied and Computational Harmonic Analysis* 46 (2) (2019) 384–399.
- [7] P. Grohs, G. Kutyniok, Parabolic molecules, *Foundations of Computational Mathematics* 14 (2) (2014) 299–337.
- [8] R. Bergmann, J. Prestin, Multivariate periodic wavelets of de la vallée poussin type, *Journal of Fourier Analysis and Applications* 21 (2) (2015) 342–369.
- [9] B. Han, Q. Mo, Z. Zhao, X. Zhuang, Directional compactly supported tensor product complex tight framelets with applications to image denoising and inpainting, *SIAM Journal on Imaging Sciences* 12 (4) (2019) 1739–1771.
- [10] T. A. Bubba, G. Kutyniok, M. Lassas, M. März, W. Samek, S. Siltanen, V. Srinivasan, Learning the invisible: A hybrid deep learning-shearlet framework for limited angle computed tomography, *Inverse Problems* 35 (6) (2019) 064002.
- [11] F. Colonna, G. Easley, K. Guo, D. Labate, Radon transform inversion using the shearlet representation, *Applied and Computational Harmonic Analysis* 29 (2) (2010) 232–250.
- [12] G. Easley, D. Labate, W.-Q. Lim, Sparse directional image representations using the discrete shearlet transform, *Applied and Computational Harmonic Analysis* 25 (1) (2008) 25–46.
- [13] E. J. King, G. Kutyniok, X. Zhuang, Analysis of inpainting via clustered sparsity and microlocal analysis, *Journal of mathematical imaging and vision* 48 (2) (2014) 205–234.
- [14] S. Yi, D. Labate, G. R. Easley, H. Krim, A shearlet approach to edge analysis and detection, *IEEE Transactions on Image Processing* 18 (5) (2009) 929–941.
- [15] S. Bonnet, A. Koenig, S. Roux, P. Hugonnard, R. Guillemaud, P. Grangeat, Dynamic x-ray computed tomography, *Proceedings of the IEEE* 91 (10) (2003) 1574–1587. doi:10.1109/JPROC.2003.817868.
- [16] T. A. Bubba, T. Heikkilä, H. Help, S. Huotari, Y. Salmon, S. Siltanen, Sparse dynamic tomography: A shearlet-based approach for iodine perfusion in plant stems, *Inverse Problems* 36 (094002) (2020).
- [17] P. S. Negi, D. Labate, 3-d discrete shearlet transform and video processing, *IEEE transactions on Image Processing* 21 (6) (2012) 2944–2954.
- [18] D. Malafronte, E. De Vito, F. Odone, Space–Time Signal Analysis and the 3D Shearlet Transform, *Journal of Mathematical Imaging and Vision* 60 (7) (2018) 1008–1024.

- [19] G. R. Easley, K. Guo, D. Labate, B. R. Pahari, Optimally sparse representations of cartoon-like cylindrical data, *The Journal of Geometric Analysis* (2020) 1–21.
- [20] K. Guo, D. Labate, The construction of smooth parseval frames of shearlets, *Mathematical Modelling of Natural Phenomena* 8 (1) (2013) 82–105. doi: 10.1051/mmnp/20138106.
- [21] D. L. Donoho, Sparse components of images and optimal atomic decompositions, *Constructive Approximation* 17 (3) (2001) 353–382.
- [22] K. Guo, D. Labate, Optimally sparse representations of 3d data with  $C^2$  surface singularities using parseval frames of shearlets, *SIAM J. Math. Analysis* 44 (2012) 851–886.
- [23] G. Kutyniok, J. Lemvig, W.-Q. Lim, Optimally sparse approximations of 3d functions by compactly supported shearlet frames, *SIAM Journal on Mathematical Analysis* 44 (4) (2012) 2962–3017.
- [24] E. M. Stein, G. Weiss, *Introduction to Fourier Analysis on Euclidean Spaces* (PMS-32), Volume 32, Princeton university press, 2016.
- [25] T. Heikkilä, 4d Cylindrical Shearlet Transform, Inverse and Adjoint for Matlab, <https://github.com/tommheik/4dCylindricalShearlet> (2021).
- [26] Y. M. Lu, M. N. Do, Multidimensional directional filter banks and surfacelets, *IEEE Transactions on Image Processing* 16 (4) (2007) 918–931.
- [27] P. J. Burt, E. H. Adelson, The laplacian pyramid as a compact image code, in: *Readings in computer vision*, Elsevier, 1987, pp. 671–679.
- [28] H. W. Engl, M. Hanke, A. Neubauer, *Regularization of inverse problems*, Springer Science & Business Media, 1996.
- [29] A. Katsevich, An accurate approximate algorithm for motion compensation in two-dimensional tomography, *Inverse Problems* 26 (6) (2010) 065007.
- [30] S. Roux, L. Desbat, A. Koenig, P. Grangea, Exact reconstruction in 2D dynamic CT: Compensation of time-dependent affine deformations, *Phys. Med. Biol.* 49 (2004) 2169–2182.
- [31] S. E. Blanke, B. N. Hahn, A. Wald, Inverse problems with inexact forward operator: iterative regularization and application in dynamic imaging, *Inverse Problems* 36 (12) (2020) 124001.
- [32] B. Hahn, Reconstruction of dynamic objects with affine deformations in computerized tomography, *Journal of Inverse and Ill-posed Problems* 22 (2014) 323–339.
- [33] B. Hahn, Null space and resolution in dynamic computerized tomography, *Inverse Problems* 32 (2016) 025006.

- [34] B. Hahn, E. Quinto, Detectable singularities from dynamic Radon data, *SIAM Journal on Imaging Sciences* 9 (2016) 1195–1225.
- [35] E. L. Ritman, Cardiac computed tomography imaging: a history and some future possibilities, *Cardiol. Clin.* 21 (4) (2003) 491–513.
- [36] M. Burger, H. Dirks, L. Frerking, A. Hauptmann, T. Helin, S. Siltanen, A variational reconstruction method for undersampled dynamic x-ray tomography based on physical motion models, *Inverse Problems* 33 (12) (2017) 124008.
- [37] J. Hakkarainen, Z. Purisha, A. Solonen, S. Siltanen, Undersampled dynamic X-ray tomography with dimension reduction Kalman filter, *IEEE Transactions on Computational Imaging* 5 (3) (2019) 492–5012.
- [38] E. Niemi, M. Lassas, A. Kallonen, L. Harhanen, K. Hämäläinen, S. Siltanen, Dynamic multi-source X-ray tomography using a spacetime level set method, *Journal of Computational Physics* 291 (2015) 218–237.
- [39] A. Hauptmann, O. Öktem, C. Schönlieb, Image reconstruction in dynamic inverse problems with temporal models, *arXiv preprint arXiv:2007.10238* (2020).
- [40] P. Chen, J. Huang, X. Zhang, A primal-dual fixed point algorithm for minimization of the sum of three convex separable functions, *Fixed Point Theory and Applications* 2016 (1) (2016) 1–18.
- [41] Z. Purisha, J. Rimpeläinen, T. Bubba, S. Siltanen, Controlled wavelet domain sparsity for x-ray tomography, *Measurement Science and Technology* 29 (1) (2017) 014002.
- [42] T. A. Bubba, T. Heikkilä, S. Siltanen, 4D dual-tree complex wavelets for time-dependent data, *arXiv preprint arXiv:2103.15674* (2021).
- [43] J. H. Jorgensen, Tomobox, <https://www.mathworks.com/matlabcentral/fileexchange/28496-tomobox>, accessed: November 6, 2018.
- [44] A. Meaney, HelTomo - University of Helsinki CT Data Toolbox, <https://www.mathworks.com/matlabcentral/fileexchange/74417-heltomo-university-of-helsinki-ct-data-toolbox>, accessed: August 20, 2020.
- [45] W. Van Aarle, W. J. Palenstijn, J. Cant, E. Janssens, F. Bleichrodt, A. Dabravolski, J. De Beenhouwer, J. Batenburg, J. Sijbers, Fast and flexible X-ray tomography using the astra toolbox, *Optics express* 24 (22) (2016) 25129–25147.
- [46] T. Heikkilä, Wavedec4 - 4D Discrete Wavelet Transform for Matlab, <https://github.com/tommheik/wavedec4> (2021).

- [47] R. Reisenhofer, S. Bosse, G. Kutyniok, T. Wiegand, A Haar wavelet-based perceptual similarity index for image quality assessment, *Signal Processing: Image Communication* 61 (2018) 33–43.
- [48] Z. Wang, A. Bovik, H. Sheikh, E. Simoncelli, Image quality assessment: from error visibility to structural similarity, *IEEE transactions on image processing* 13 (4) (2004) 600–612.
- [49] Z. Wang, E. Simoncelli, A. Bovik, Multiscale structural similarity for image quality assessment, in: *The Thirty-Seventh Asilomar Conference on Signals, Systems & Computers, 2003, Vol. 2, Ieee, 2003*, pp. 1398–1402.
- [50] Z. Wang, L. Lu, A. Bovik, Video quality assessment based on structural distortion measurement, *Signal processing: Image communication* 19 (2) (2004) 121–132.
- [51] C. Bampis, Z. Li, A. Bovik, Spatiotemporal feature integration and model fusion for full reference video quality assessment, *IEEE Transactions on Circuits and Systems for Video Technology* 29 (8) (2018) 2256–2270.
- [52] L. Chow, R. Paramesran, Review of medical image quality assessment, *Biomedical signal processing and control* 27 (2016) 145–154.